Supporting Information

Linker Exchange via Migration along Backbone in Metal-Organic Frameworks

Nader Al Danaf,[†] Waldemar Schrimpf,[†] Patrick Hirschle,[†] Don C. Lamb,[†] Zhe Ji,[*,‡,§] and Stefan Wuttke,[*,†,∥,⊥]

[†] Department of Chemistry and Center for NanoScience, University of Munich, Butenandtstraße 5-13, 81377 Munich, Germany.

[‡] Department of Chemistry, University of California-Berkeley, Berkeley, California 94720.

[§] Present address: Department of Chemistry, Stanford University, Stanford, California 94305.

[∥] BCMaterials (Basque Center for Materials, Applications & Nanostructures), Bldg. Martina Casiano, 3rd. Floor, Barrio Sarriena s/n, 48940, Leioa, Spain.

[⊥] IKERBASQUE, Basque Foundation for Science, 48009 Bilbao, Spain.

* zhej@stanford.edu, stefan.wuttke@bcmaterials.net

Table of Contents

1. Experimental Section

1.1. Chemicals and supplies.

Anhydrous N,N-dimethylformamide (DMF), anhydrous methanol, and glacial acetic acid were obtained from EMD Millipore Chemicals. Ethyl acetate (99.9%, HPLC Plus), ethanol (≥ 99.5%, ACS Reagent), isopropyl alcohol (≥ 99.5%, BioReagent), tetrahydrofuran (THF, ≥ 99.9%, for high performance liquid chromatography (HPLC)), nitric acid (70%, ACS Reagent), sulfuric acid (95.0–98.0%, ACS Reagent), hydrochloric acid (37%, ACS Reagent), sulfuric acid (95.0–98.0%, ACS Reagent), hydrochloric acid (37%, ACS Reagent), sodium bicarbonate (BioReagent), sodium sulfate (≥ 99.0, ACS Reagent), palladium on carbon (Pd/C, 10 wt.% loading), potassium hydroxide (90%), zirconium chloride ((≥ 99.5%, trace metal basis), BPDC (97%), dimethyl biphenyl-4,4'- dicarboxylate (99%), and rhodamine B-isothiocyanate (RB, mixed isomers) were obtained from Sigma-Aldrich. Ultra-high-purity grade H_2 gas (Praxair, 99.999% purity) was used for the hydrogenation reaction. All starting materials, reagents, and solvents were used without further purification.

1.2. Synthesis of dye-functionalized linkers.

The dye-modified linkers were synthesized in a multi-step procedure (Fig. S1). The synthesis procedure is illustrated in Figure S1. Dimethyl 2-nitrobiphenyl-4,4'-dicarboxylate (II): A solution of 10 g (37 mmol) of dimethyl biphenyl-4,4'-dicarboxylate (I) in 100 mL of concentrated sulfuric acid was cooled to 0 °C and a mixture of 5 mL of 58% nitric acid and 7.5 mL of concentrated sulfuric acid was added dropwise over a period of 30 min under stirring, maintaining the temperature at 0–5 °C. The mixture was then stirred for 1 h at 0–5 °C, diluted with 100 mL of water, and extracted with ethyl acetate. The extract was washed with water and a solution of sodium bicarbonate (7.5%), dried over anhydrous sodium sulfate and evaporated. The residue was recrystallized from isopropyl alcohol. Yield: 9.9 g (31 mmol, 85%). 1H NMR (600 MHz, $CDCl_3$), parts per million [p.p.m.]: 3.98 (s, 3H), 4.02 (s, 3H), 7.43 (d, *J* = 8.4 Hz, 2H), 7.57 (d, *J* = 8.0 Hz, 1H), 8.14 (d, *J* = 8.4 Hz, z2H), 8.32 (dd, *J* = 8.0, 1.7 Hz, 1H), 8.58 (d, *J* = 1.7 Hz, 1H) (Fig. S2).

Dimethyl 2-aminobiphenyl-4,4'-dicarboxylalte (III): A mixture of 9.9 g (31 mmol) of compound II, 100 mL of acetic acid, and 5 g of 10% Pd/C in a high-pressure reactor was hydrogenated at room temperature using a hydrogen pressure of 10–50 atm until hydrogen was no longer consumed. The mixture was filtered and acetic acid in the filtrate was removed under vacuum. The crude product was recrystallized from ethanol. Yield: 8.8 g (29 mmol, 94%). 1H NMR (600 MHz, $CDCl_3$), [p.p.m.]: 3.93 (broad s, 2H), 3.94 (s, 3H), 3.98 (s, 3H), 7.21 (d, *J* = 8.0 Hz, 1H), 7.47 (d, *J* = 1.6 Hz, 1H), 7.51 (dd, *J* = 8.0, 1.6 Hz, 1H), 7.58 (d, *J* = 8.5 Hz, 2H), 8.15 (d, *J* = 8.5 Hz, 2H) (Fig. S3).

2-Aminobiphenyl-4,4'-dicarboxylic acid (NH_2-BPDC, IV): A solution of 4.95 g (20 mmol), compound III, in THF (180 mL) and MeOH (130 mL) was mixed with a solution of potassium hydroxide (10 g, 178 mmol) in water (200 mL). The reaction mixture was heated and allowed to reflux overnight. After all the volatiles were removed under vacuum, it was diluted with 200 mL of water, and acidified with 6 M hydrochloric acid until a pH value of 2 was obtained. The precipitates were collected, washed with water and dried in air. The yield was 4.3 g (17 mmol, 85%). 1H NMR (400 MHz, dimethyl sulfoxide-d6 (DMSO-d6)), [p.p.m.]: 5.18 (s, 2H), 7.11 (d, *J* = 7.9 Hz, 1H), 7.21 (dd, *J* = 7.9 Hz, 2H), 7.41 (s, 1H), 7.57 (d, *J* = 8.3 Hz, 2H), 8.01 (d, *J* = 8.3 Hz, 2H), 12.84 (s, 2H) (Fig. S4).

2-RhodamineB-isothiocyanate-biphenyl-4,4'-dicarboxylic acid (BPDC-RB, VI): A solution of 0.25 g (0.95 mmol) of compound IV in DMF (5 mL) was added to 0.51 g (0.95 mmol) of Rhodamine B isothiocyanate (RB, mixed isomers, V). The reaction solution was stirred for 24 h at room temperature. The mixture was then diluted with 100 mL of 1 M hydrochloric acid. The precipitates were collected by filtration, washed with water and dried in air. The crude product was subjected to purification by HPLC preparation (stationary phase: C18; mobile phase: MeOH/water/0.1% TFA). The eluent was freeze-dried and the orange solid was collected. The yield was 0.30 g (0.36 mmol, 38%). MS (ESI+, m/z): [M] calculated for $C_{43}H_{41}O_7N_4S^+$, 757.27; found, 757.30.

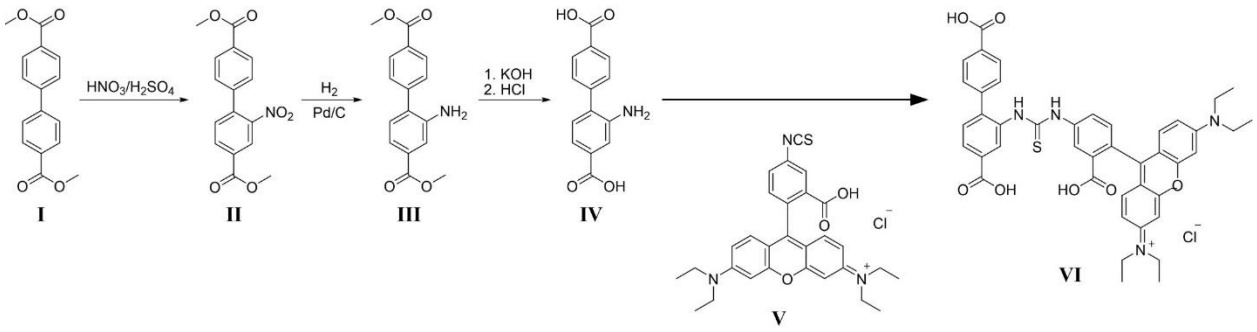

Figure S1: Synthetic pathway to the BPDC-RB linker.

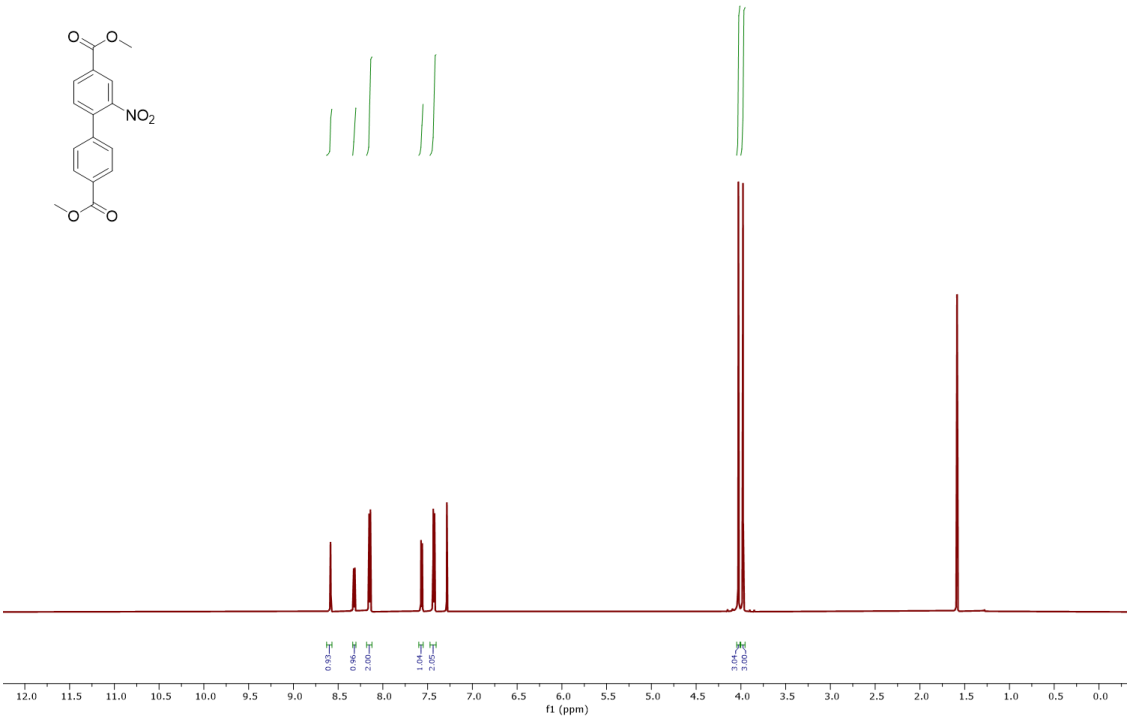

Figure S2: Liquid ^{1}H NMR spectrum of dimethyl 2-nitrobiphenyl-4,4'-dicarboxylate in $CDCl_3$.

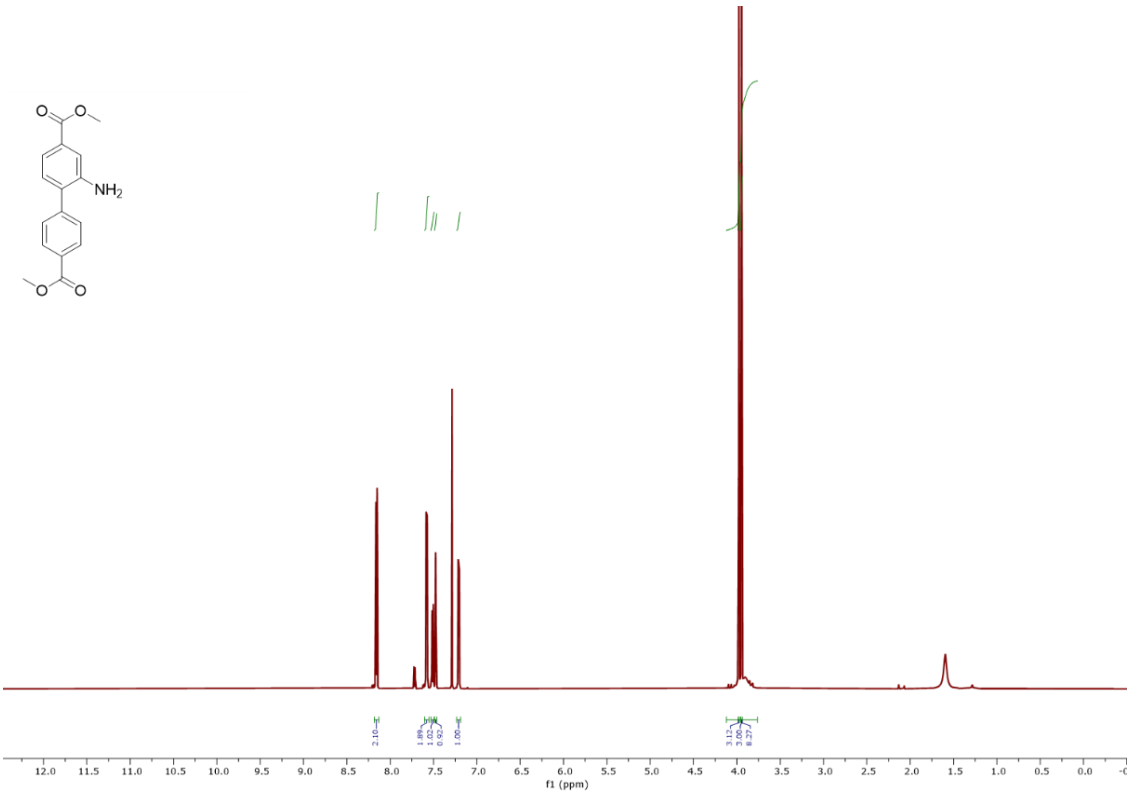

Figure S3: Liquid ^{1}H NMR spectrum of dimethyl 2-aminobiphenyl-4,4'-dicarboxylalte in $CDCl_3$.

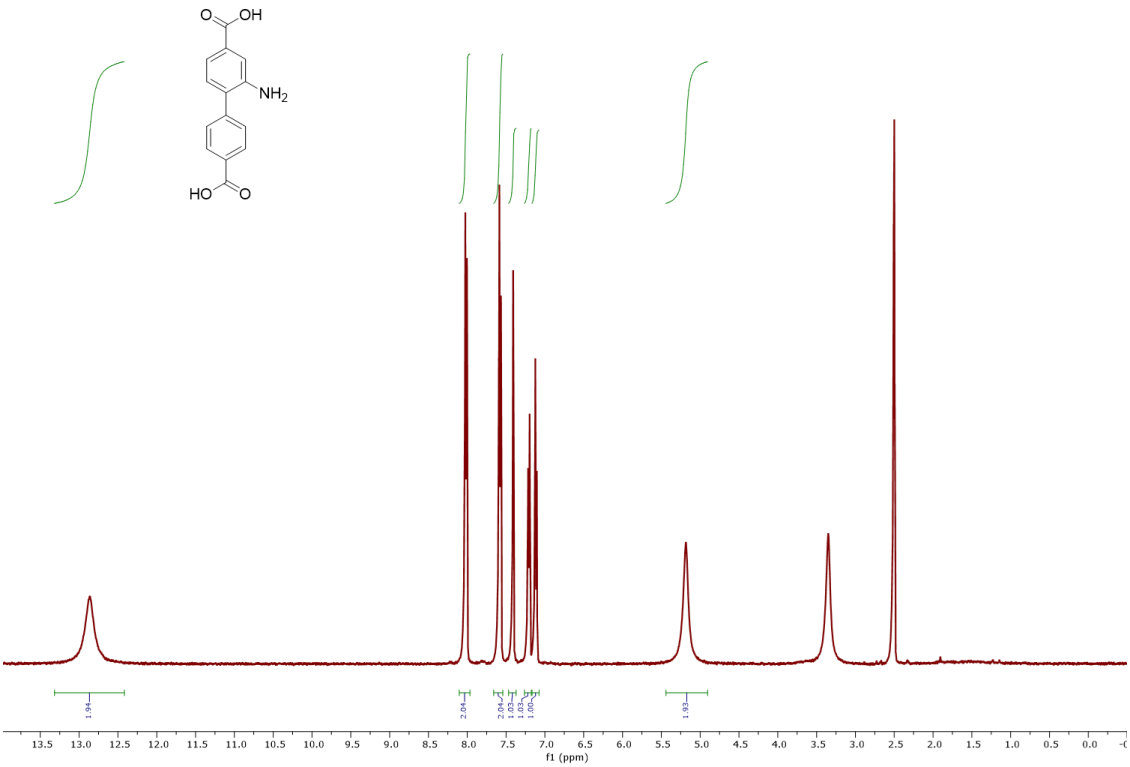

Figure S4: Liquid ^{1}H NMR spectrum of 2-aminobiphenyl-4,4'-dicarboxylic acid in DMSO-d6.

1.3. Synthesis of large crystal UiO-67.

Large, single UiO-67 crystals were synthesized following the procedure of Ko et al.[1] A mixture of BPDC (85 mg, 0.35 mmol), zirconium(IV) chloride (82 mg, 0.35 mmol) and benzoic acid (1.28 g, 10.5 mmol) was dissolved in DMF (20 mL) in a 20 mL vial. The vial was capped and heated in an isothermal oven at 120 °C for 2 days to yield octahedral-shaped crystals of ~ 50 µm diameter. The reaction mixture was allowed to cool down to room temperature and then washed with DMF (three times per day for 3 days) and acetone (three times per day for 3 days). The solvent exchanged samples were then evacuated at 120 °C to 30 mTorr.

1.4. Post-synthetic linker exchange (PSE).

The fluorophore-labelled linker (2-amino-biphenyl-4,4'-dicarboxylic acid labelled with rhodamine B isothiocyanate, BPDC-RB) was incorporated into UiO-67 via a solvothermal approach: Each sample was prepared by immersing UiO-67 (~3 mg) with BPDC-RB (0.1 mg/mL) in DMF or a 20% DMF / 80% MeOH mixture using a tightly capped 25 ml glass bottle (classic version Duran bottle, Schott) for the reaction. This reaction mixture was incubated for four different time periods: 1 day and 7 days at RT and 1 day and 7 days at 100 °C in a glass reactor (Scheme S1). Subsequently, the resulting product was washed via centrifuging (2000 rpm, 3 min) first with DMF (3 x 5 mL) and then with MeOH (3 x 5 mL). Afterwards, the samples were dried at 70 °C for 8 hours.

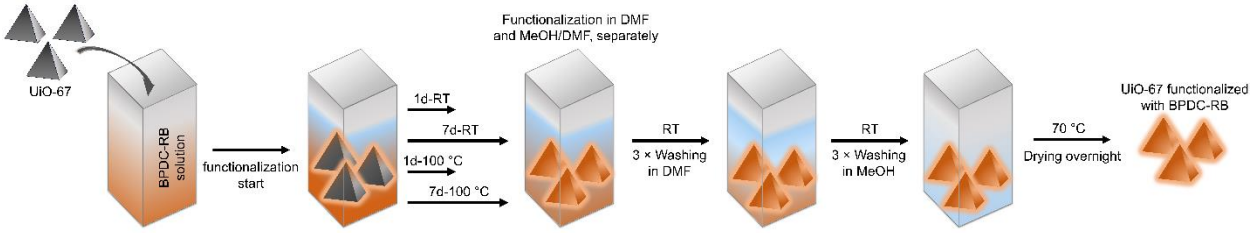

Scheme S1: Schematic representation showing the procedure followed to functionalize the UiO-67 samples with BPDC-RB.

1.5. Fluorescence measurements on digested UiO-67 crystals.

The fraction of dyes in the UiO-67 samples was determined via fluorimetry. The incorporated BPDC-RB within the UiO-67 framework was set free via incubation of the host-particles in a digestion solution. For the different functionalization experiments, 0.25 mg per condition was used, where the respective samples were given to a mixture of CsF (0.23 mol/L) in DMSO/H_2O (3 mL), in a ratio of 9:5 DMSO/H_2O (v/v). The samples were then sonicated for 30 minutes leading to the destruction of the UiO-67. The digested samples were allowed to sit for two hours after which bulk fluorescence experiments were performed to determine the amount of incorporated BPDC-RB linker and the exchange ratio observed for the different PSE conditions.

Measurements were done on an FLS 1000 Fluorimeter (Edinburgh Instruments). A pulsed laser diode at 561 nm (LDH-FA-560, PicoQuant) was used for measuring the different emission spectra and the bulk lifetime measurements. The fluorescence emission was recorded using a photon multiplier tube (PMT 900 detector, Hamamatsu) and the lifetime decays were measured on a high speed PMT (H10720-01 High speed PMT, Hamamatsu) using a laser repetition rate of 32 MHz. The digested UiO-67 samples were measured in a 3.5 mL quartz cuvette (119F-10-40, Hellma Analytics). For the emission spectra, a 1 nm emission slit width and an excitation power of 1 mW were used. The spectra were recorded in 0.5 nm steps with 0.5 seconds acquisition time per step across the spectral range of interest. The fluorescence lifetime measurements were performed using time-correlated single-photon counting (TCSPC), where the raw

lifetime data and subsequent lifetime fits resulted in a single exponential decay. The lifetime fits were obtained according to the following equation:

$$I(t) = I_0 e^{-\frac{t}{\tau}} + c$$

where τ is the decay lifetime with I_0 being the decay intensity at t = 0 and c being the offset value relative to I_0. The lifetime fits were performed with our home written software PIE analysis with Matlab (PAM). PAM is a stand-alone program (MATLAB; The MathWorks GmbH) for integrated and robust analysis of fluorescence ensemble, single-molecule, and imaging data.[2]

1.6. Fluorescence intensity and fluorescence lifetime imaging microscopy (FLIM).

Fluorescence intensity and lifetime measurements were performed using a house-built laser scanning confocal microscope equipped with pulsed interleaved excitation and TCSPC detection, as described elsewhere with a few modifications.[3] Briefly, a pulsed laser diode at 561 nm wavelength (LDH-FA-560, PicoQuant) driven by a laser driver (PDL 828 Sepia II, PicoQuant) at 40 MHz was used for excitation of the BPDC-RB functionalized UiO-67. For the measurements, the UiO-67 powder was suspended in water and vortexed for ~3 min. From the suspension, ~ 30 µL was added to an 8-well LabTek I slide (VWR) and the UiO-67 fragments allowed to sediment. The surface was imaged using a 60x, 1.27 numerical aperture water-immersion objective (Plan Apo IR × 60 WI, Nikon). The fluorescence emission was collected with the same objective, separated from the excitation using a polychroic mirror (Semrock Di01-R405/488/561/635, AHF Analysentechnik, Tübingen, Germany) and a 595/50 nm long pass filter (ET 595/50, Chroma), and recorded using a single photon avalanche photodiode (SPCM-AQR-14, Perkin-Elmer). Typical scan regions were between 60 µm × 60 µm and 90 µm × 90 µm, depending on the size of the measured UiO-67 crystal. Scans were performed with a pixel size of 200 nm, resulting in images between 300 × 300 pixels and 450 × 450 pixels. The fluorescence intensity images were collected at different depths within the crystal with 500 nm separation between the different planes providing the three-dimensional intensity distribution of the crystals. For FLIM, scans were performed at the surface, and at 2 µm and 4 µm above surface with image acquisition times of 200-400 s to ensure the detection of 200-1000 photons per pixel. To ensure a good signal-to-noise ratio while minimizing the influence of photon pile-up and other high-signal artifacts, the count rate was kept below 1000 kHz. The desired count rate was achieved by adjusting the power of the 561 nm wavelength laser using a neutral density filter-wheel (NDC-100C-2M, Thorlabs). Laser power ranged from 5 to 500 nW measured before the objective (S130VC Slim Photodiode Power Sensor, Thorlabs). A phasor analysis[4-5] was applied to the data using our software framework PAM.[2] To improve the FLIM analysis, the data were spatially smoothed with a 3 pixel × 3 pixel sliding window.

The FLIM phasor approach, as described by Digman and co-workers,[5] allows a graphical interpretation of the measured fluorescence lifetime, thus avoiding a more complicated fit-based analysis that can result in a biased interpretation of the data when a wrong fit model is used. From the FLIM measurements, the sine and cosine Fourier components of the lifetime decay are calculated for every pixel in an image, yielding the two phasor coordinates *g* and *s*:

$$g_{i,j}(\omega) = \frac{\int_0^{2\pi} I_{i,j}(t) \cdot cos(\omega t - \varphi_{Inst})\, dt}{\left(M_{Inst} \cdot \int_0^{2\pi} I_{i,j}(t) dt\right)}$$

$$s_{i,j}(\omega) = \frac{\int_0^{2\pi} I_{i,j}(t) \cdot sin(\omega t - \varphi_{Inst})\, dt}{\left(M_{Inst} \cdot \int_0^{2\pi} I_{i,j}(t) dt\right)}$$

where the indices *i* and *j* define the pixel of the image and $I_{i,j}(t)$ gives the photon counts of the time bin, *t,* of the lifetime decay histogram of the corresponding pixel. The frequency, ω, corresponds to $2\pi/T$ where *T* is the full timescale of the lifetime decay histogram (here 40 ns). φ_{Inst} and M_{Inst} are correction terms for the phase shift and demodulation caused by the instrument response function. The correction terms were calculated using a reference sample with known lifetime (Atto 565, 4.0 ns, Atto-Tec).

From the two phasor coordinates, two lifetime values can be determined, one based on the phase (τ_φ) and the second on the modulation (τ_M):

$$\tau_\varphi(\omega) = \frac{1}{\omega} \cdot \frac{s}{g} \quad \text{and} \quad \tau_M(\omega) = \frac{1}{\omega}\sqrt{\frac{1}{g^2+s^2} - 1}$$

For a purely mono-exponential decay, these two lifetimes are identical and correspond to the correct lifetime. In the case of multi-exponential components, the phase and modulation lifetimes are different and do not correspond directly and unambiguously to the pure species. In the phasor approach, multiple species will be added vectorially. For example, a mixture of two species with different mono-exponential lifetimes will lie on a line connecting the individual components of the two species on the unit circle. Where the mixture falls on this line depends on the relative population of the two species. To get a single apparent lifetime for each sample, the mean τ_φ and τ_M were calculated from all pixels above a threshold of ~ 200 photons. The arithmetic average of the mean phase and modulation lifetimes was then used to calculate an apparent lifetime. The uncertainty corresponds to the standard deviation of the pixel distribution.

1.7. Powder X-ray diffraction (PXRD).

PXRD measurements were conducted on a Bruker D8-Venture diffractometer with a Mo-target (0.71073 Å) and Cu-target (1.54184 Å) microfocus X-ray generators. The theta-theta geometry device was equipped with a PHOTON-100 CMOS detector, measuring the samples between 2° and 50° 2θ, with a step-size of 0.02° 2θ.

1.8. Scanning electron microscopy (SEM).

A Zeiss NVision40 microscope was used to record SEM images. Secondary electron images were acquired using the InLens detector at a low acceleration voltage of 5 kV. To avoid charging effects, a thin carbon film coating was applied on the samples before the measurements. The carbon deposition was performed using a BAL-TEC coating system.

1.9. Thermogravimetric analysis (TGA).

A Netzsch Jupiter ST 449 C instrument equipped with a controller (Netzsch TASC 414/4) was used to determine the missing linker defects within the pristine UiO-67. A sample of ~ 8 mg pristine UiO-67 was loaded into an aluminum oxide crucible and heated from the range of 25 °C to 900 °C at a heating rate of 10 °C/min under synthetic air flow conditions (containing ~ 21% O_2 from the air liquid supplier).

2. Precluding the possibility of through-window diffusion

2.1. Estimation of the size of guest molecules.

To estimate the size of the guest molecules, their geometries were optimized using density functional theory (DFT) at the b3lyp/6-311++g(2d,2p) level. Multiple orientations of these molecules were sampled to identify the one with the smallest projection areas. For this particular orientation, the longest distance spanning the molecule represents its size. If this size is smaller than a pore window, the guest molecule can pass through the window. The structures, orientations, and sizes of the guest molecules are depicted in Fig.S5. The sizes of fluorescein, rhodamine b isothiocyanate (RB), and BPDC-RB is 11.6 Å, 15.2 Å, and 15.8 Å, respectively. The edge length of the triangular window of UiO-67 is ~12 Å. Based on these results, we predicted that only fluorescein is able to pass through the window, while RB and BPDC-RB are unable to penetrate UiO-67 crystals via through-window diffusion.

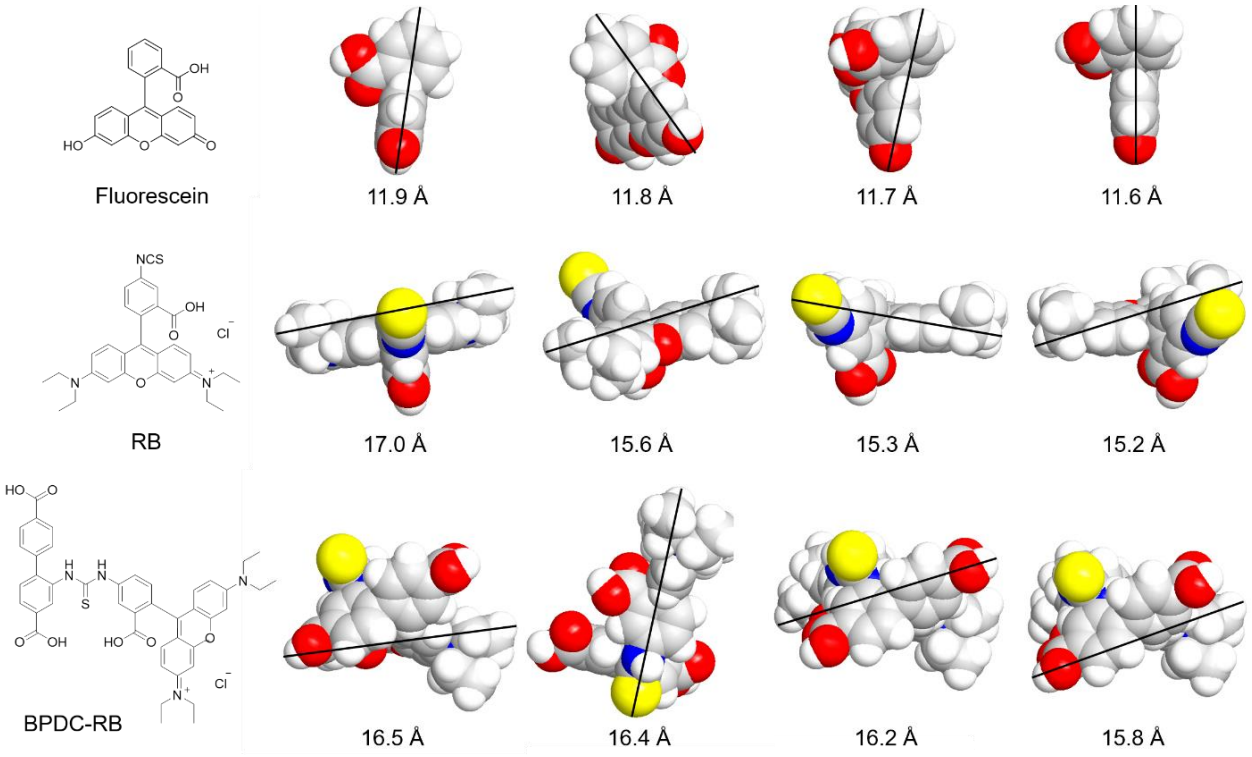

Figure S5: The structure and Van der Waal models for the guest molecules. From left to right, the structure followed by four projections of fluorescein (upper row), RB (middle row) and BPDC-RB (bottom row) are shown. The projection radius decreases and the orientation on the right end presents the minimum size of the molecule.

2.2. Penetration test using fluorescence imaging.

Our prediction on the penetrability of fluorescein and RB was confirmed by soaking UiO-67 in solutions of the two fluorophores for 7 days at RT in DMF. As we expected, after soaking with RB, no fluorescence signal was observed in the interior of the crystal, while the surface of the crystal shows high fluorescence intensity (Fig.S6). In contrast, soaking with fluorescein led to deep penetration of the dye into the MOF. This observation confirms that RB is too large to pass through the window of UiO-67, while fluorescein, a smaller dye, can pass through the window and exhibits through-window diffusion behavior. Considering that BPDC-RB is even larger than RB, it cannot pass through the window as well. This matches with the result of a penetration test of BPDC-RB under the same condition (see Fig. S14), which displayed no

penetration. Therefore, we postulate that the unusual penetration of BPDC-RB, when MeOH/DMF is used as the incubation solvent, must indicate a penetration mechanism other than through-window diffusion.

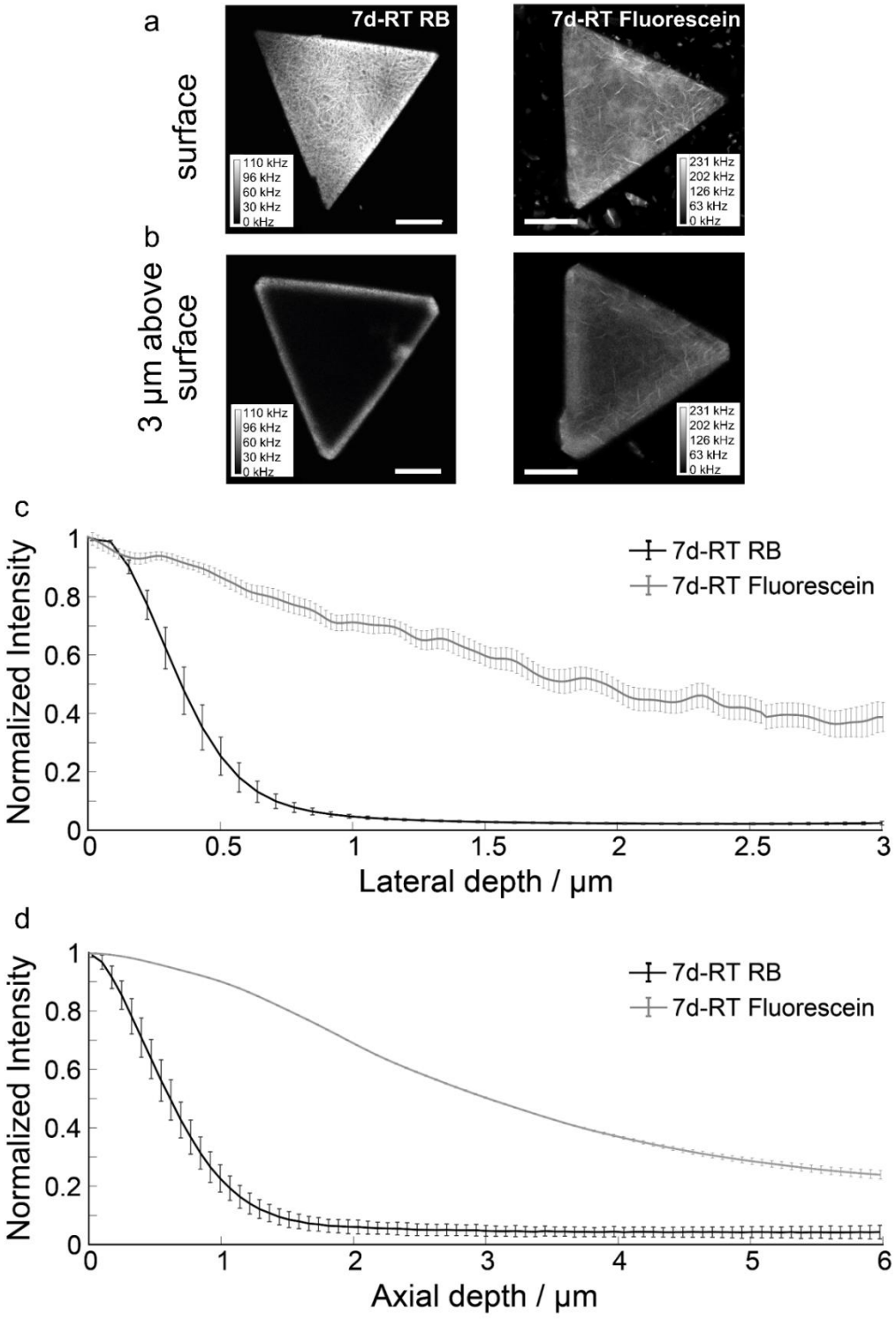

Figure S6: Fluorescence imaging of UiO-67 crystals after incubation with RB and fluorescein for 7 days at RT in DMF. **a**) Fluorescence images of a UiO-67 crystal taken at the surface and (**b**) 3 µm above the surface. The scale bars are 15 µm. **c**) The fluorescence intensity profile along lateral direction 3 µm above the surface and (**d**) in the axial direction. Error bars are determined from measurements on 3 crystals of UiO-67 per condition.

2.3. Analysis of missing-linker defects in pristine UiO-67.

Although the size of UiO-67 window is ~12 Å, the presence of missing-linker defects can create windows of larger sizes. These larger-sized windows could allow for the otherwise forbidden through-window diffusion across the defect sites. To preclude the possibility that missing-linker defects present in pristine UiO-67 alter the diffusion behavior of BPDC-RB, we analyzed the number of missing-linker defects present in our UiO-67 crystals and evaluated their impact.

We employed TGA to calculate the defect level. As shown in Fig. S7, a loss of 4.3% of the mass before 275 °C can be ascribed to the leaving of adsorbed moisture, benzoate, and formate ligands, and to the dehydration of the Zr cluster, according to

$$Zr_6O_4(OH)_4(BPDC)_x(benzoate)_y(formate)_z \rightarrow Zr_6O_6(BPDC)_x, \qquad x + 0.5y + 0.5z = 6.$$

The remaining loss of 61.7% of the mass is due to the decomposition of BPDC from 400 °C to 660 °C, which leaves the remaining 34.0% of the mass to be ZrO_2, according to:

$$Zr_6O_6(BPDC)_x \rightarrow 6\ ZrO_2.$$

Based on the loss of mass and the molecular weight of the leaving components, we calculated x = 5.99, indicating a very low level of missing-linker defects (0.01 out of 6).

In the above calculation, we assume that the amount of missing-cluster defects is negligible, as we do not observe any forbidden low-angle reflections in PXRD (see Fig. S9).

Compared with literature,[6] our TGA matches very well with those obtained for defect-free UiO-67 samples.

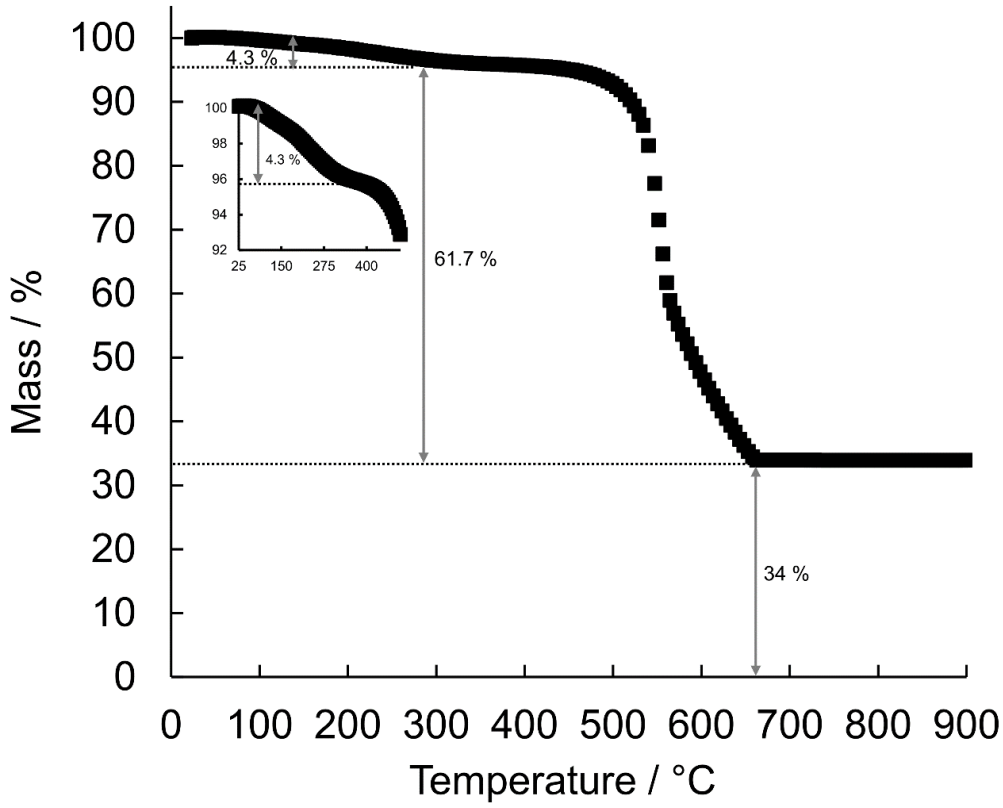

Figure S7: TGA of pristine UiO-67 crystals.

3. Single-crystal characterization

In this study, the spatial and mechanistic aspects of PSE were investigated in a prototypical zirconium-based MOF. For this, large UiO-67 crystals, ~50 µm in diameter, were synthesized and subsequently functionalized with fluorescently labeled linkers using linker exchange. The fluorophore served hereby as a probe for investigating the spatial and mechanistic progression of PSE. It has been demonstrated that this MOF prototype is as a robust platform for PSE due to its unique thermal and chemical stability.[7] Consequently, the large UiO-67 crystals were chosen to provide a three dimensional scaffold that includes tetrahedral and octahedral pores, where the later are large enough for the fluorescently labeled linker to get incorporated in the UiO-67 lattice without altering its topology.

Prior to the PSE studies, additional experiments were performed to characterize the autoluminescence properties of the pristine UiO-67 crystals. In this regard, the fluorescence properties of the UiO-67 crystals (*i.e.* the autofluorescence intensity and autofluorescence lifetime) were determined. We observed a weak autofluorescence signal, which would correspond to ~ 5 kHz during our measurements with BPDC-RB (which is a factor of 20x to 100x less than the intensity obtained for the different PSE conditions investigated) via direct excitation at 561 nm (Fig. S8 a and b). Similarly, the direct excitation of the pristine UiO-67 exhibited an autofluorescence lifetime of ~ 3.3 ns (Fig S8 c and d).

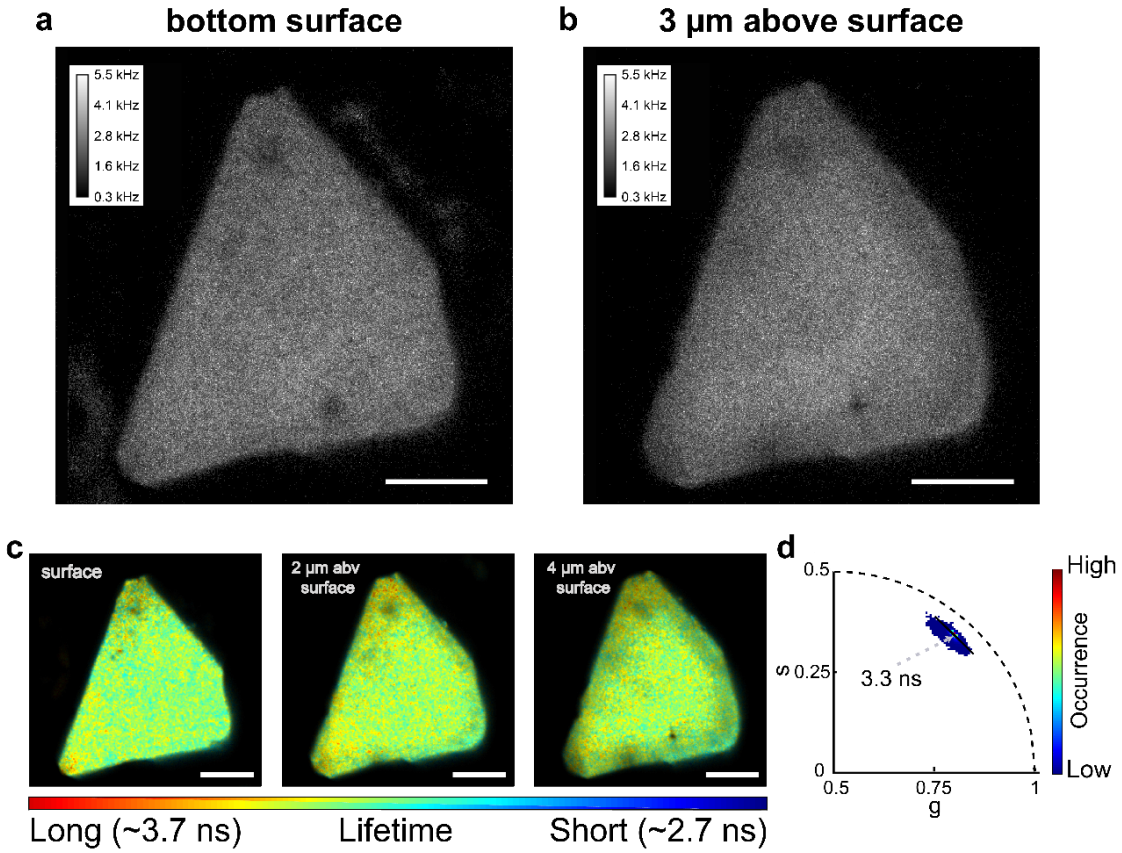

Figure S8: Autofluorescence intensity and lifetime of pristine UiO-67 via direct excitation at 561 nm. **a**) Fluorescence images taken at the surface and (**b**) 3 µm above the surface. **c**) FLIM images and **d**) the corresponding phasor plot of the three FLIM images in panel **c**. The color in the phasor plots corresponds to the number of pixels exhibiting the phasor value (blue indicating the lowest occurrence and red indicating the highest occurrence); see color bar. The scale bar is 15 µm.

The BPDC-RB was incubated with UiO-67 in either a solution of 80% methanol / 20% DMF v/v (for brevity, this mixture is further on referred to as MeOH/DMF) or alternatively in DMF alone. We performed the UiO-67 functionalization with BPDC-RB under four different conditions for each medium (as shown in Scheme 1): 1 day and 7 days at RT (referred to as 1d-RT and 7d-RT), and similarly 1 day and 7 days at

100 °C (referred to as 1d-100 °C and 7d-100 °C). PXRD and SEM showed that the treatment did not alter the morphology and crystallinity of the functionalized UiO-67 crystals (Fig.S9).

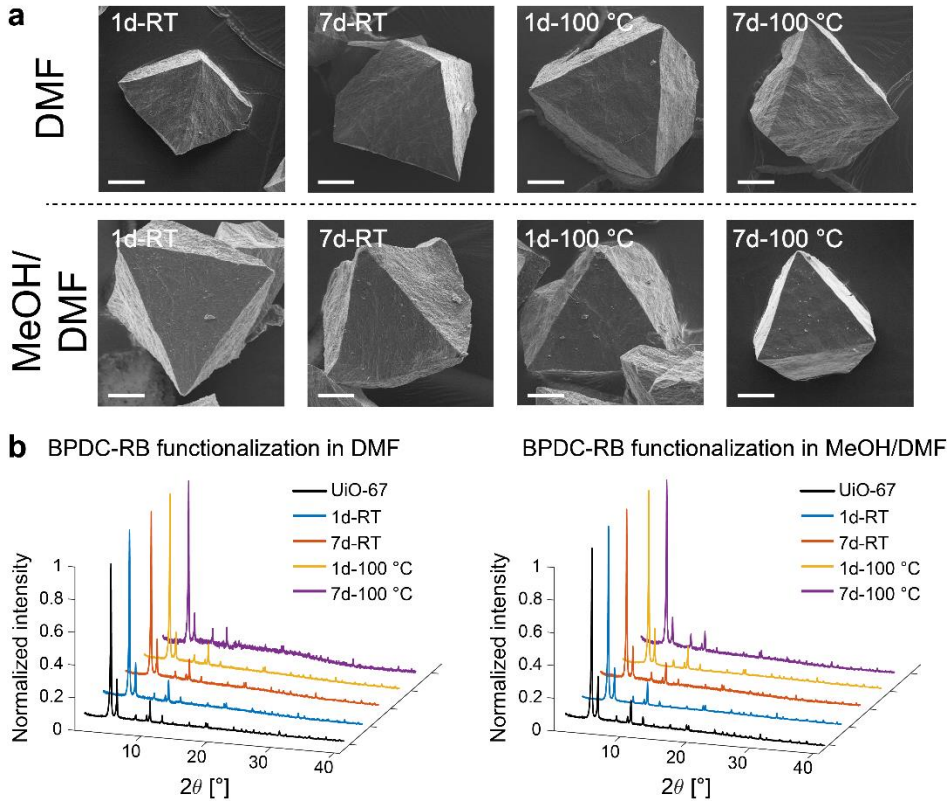

Figure S9: SEM images and XRD patterns of the different UiO-67 samples after PSE. **a**) SEM images of UiO-67 crystals in DMF (upper row) and MeOH/DMF (lower row). **b**) PXRD spectra of UiO-67 crystals in DMF (left) and MeOH/DMF (right).

4. Bulk fluorescence measurements.

4.1. Examination of photophysical damage to BPDC-RB under PSE conditions.

After UiO-67 functionalization with BPDC-RB, we observed a color change on the UiO-67 solid samples. All reactions performed in DMF resulted in a pale pinkish color while, in MeOH, a clear, gradual, color shift from light pink (1d-RT) to dense red (7d-100 °C) was observed (Fig.S10 a), which is the first indication that linker exchange in MeOH/DMF is significantly faster than in DMF.

Before performing the single crystal fluorescence studies, we characterized the fluorescence properties in bulk. These control experiments were conducted to investigate the photophysical properties of free BPDC-RB and those released from the digested UiO-67. Also, we investigated whether the change in color from the different incubation conditions correlates the overall fluorescence emission of the BPDC-RB and the degree of PSE observed. For this purpose, 0.25 mg/mL of UiO-67 crystals (solid) were digested in a DMSO/H_2O solution containing CsF and characterized in bulk solution using a fluorimeter (Fig.S10 b and Section S1.5). After the digestion of the UiO-67 crystals, the fluorescence emission and lifetime were characterized.

The fluorescence intensity observed for the digested UiO-67 functionalized in MeOH/DMF showed a noticeably higher amount of BPDC-RB compared to DMF (Fig.S10 c, e, and g). However, in both incubation media, the extent of linker exchange showed a similar trend (*i.e.* more BPDC-RB with increasing the incubation time and temperature). For comparison, we measured the spectrum of UiO-67 in the absence of a fluorescence linker, which showed a minor Raman peak at 582 nm which is also observable for UiO-67 functionalized in DMF (Fig.S10 c). The emission maxima of BPDC-RB in DMF was observed to be around 578 to 580 nm (Fig.S10 c). A similar fluorescence emission behaviour was observed for UiO-67 functionalized in MeOH/DMF with a slight bathochromic shift of the emission maxima ranging between 580 and 582 nm (Fig.S10 e).

Furthermore, we measured the lifetimes of BPDC-RB after digesting the functionalized UiO-67 to check whether the different PSE conditions resulted in alterations in the fluorescence properties of the fluorophores themselves. For both media and all four conditions, the resulting lifetimes were very similar (2.14-2.15 ns) indicating that the handling of the MOFs did not affect the fluorescence properties. (Fig.S10 d, f, and Table S1).

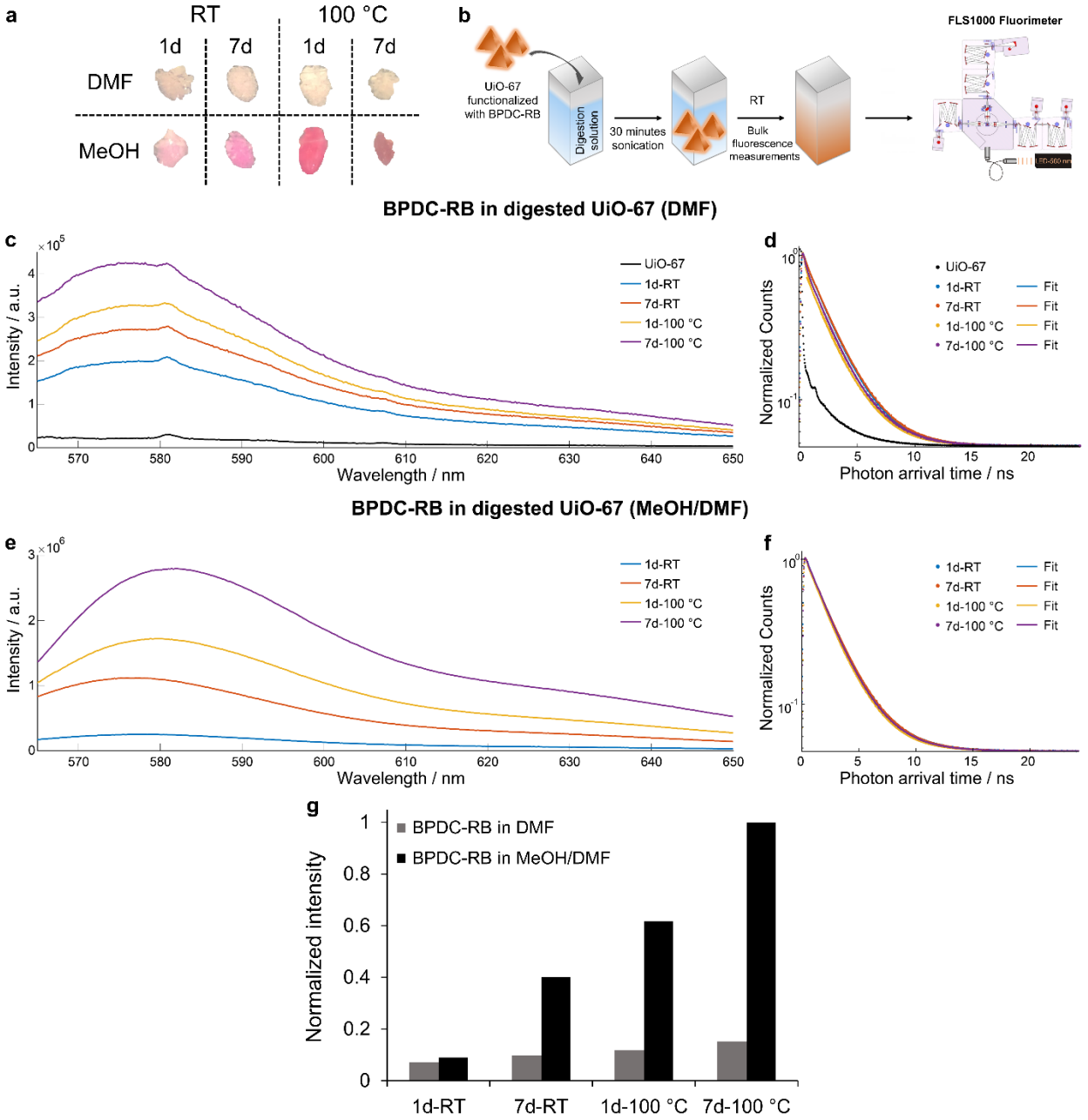

Figure S10: Bulk observations and fluorescence characterization of the different UiO-67 samples after PSE in DMF and MeOH/DMF. **a**) Optical images of the solid UiO-67 samples showing the change in color upon PSE. **b**) Schematic presentation of the steps for digesting the UiO-67 and performing the fluorescence measurements. **c)** The fluorescence emission and **d**) lifetime decays for the digested UiO-67 in DMF. **e**) The fluorescence emission and **f**) lifetime decays for the digested UiO-67 after PSE in MeOH/DMF. **g**) Normalized intensity values for the BPDC-RB in the digested UiO-67 relative to the fluorescence intensity (at $\lambda_{emission}$ maximum) of the digested UiO-67 after PSE for 7d-100 °C in MeOH/DMF.

Similarly, the BPDC-RB lifetime behaviour was investigated, to make sure that the lifetime differences within the UiO-67 crystals are due to the local nano-environment changes owing to the PSE and not the degradation of the fluorophore itself. Here, the BPDC-RB lifetime (alone, in the absence of any MOF) was investigated under the four different incubation conditions (1d-RT, 7d-RT, 1d-100 °C and 7d-100 °C) in DMF and MeOH/DMF, respectively. The obtained BPDC-RB lifetimes are 2.30 ± 0.06 ns in DMF (Fig.S11 and Table S1) and 2.23 ± 0.10 ns in MeOH/DMF (Fig.S12 and Table S1). The measured lifetimes of the

BPDC-RB alone showed a monoexponential lifetime decay under the four different conditions tested, which confirmed the absence of an unexpected dye photophysical behaviour that might influence lifetime measurements in the single UiO-67 crystals.

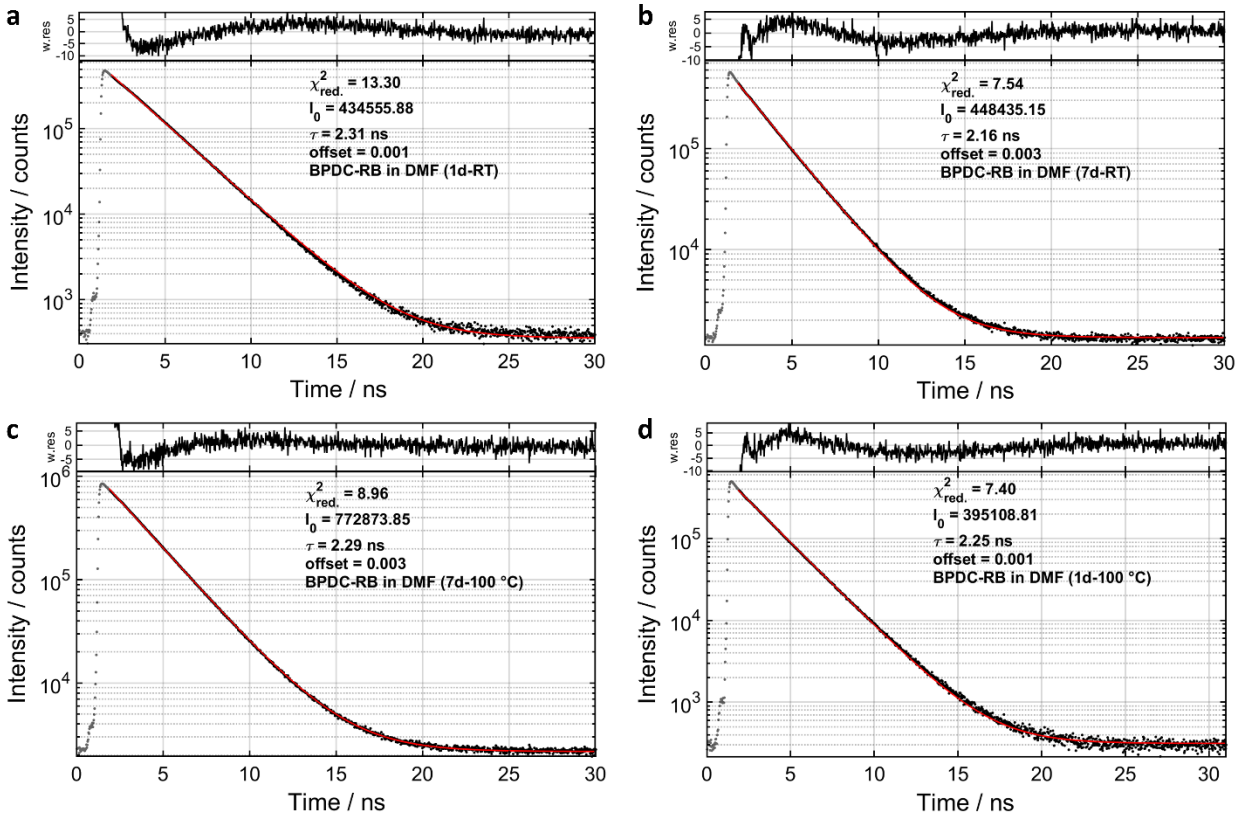

Figure S11: Fluorescence lifetime decay data and fits obtained for the BPDC-RB (alone) investigated under similar conditions used for PSE in DMF **a**) for 1d-RT, **b**) for 7d-RT, **c**) for 1d-100 °C and **d**) for 7d-100 °C.

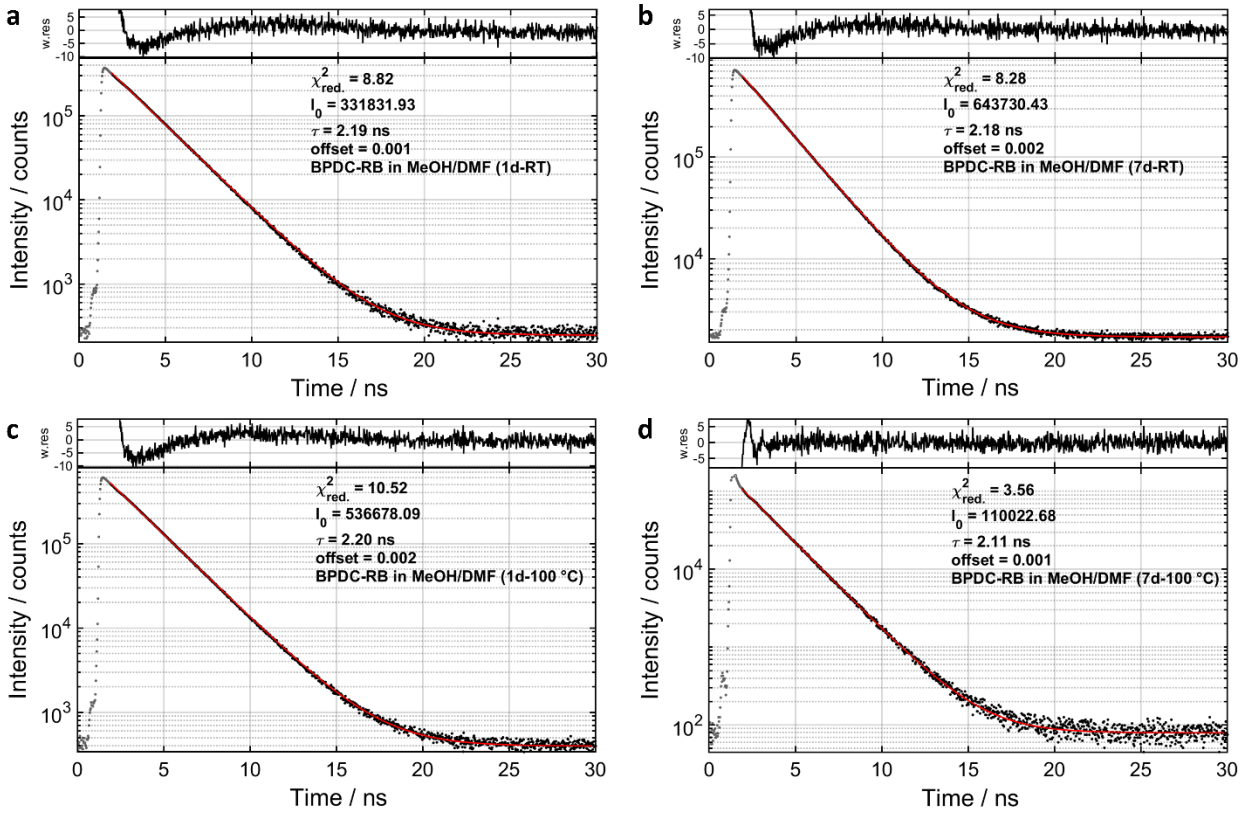

Figure S12: Fluorescence lifetime decay data and fits obtained for the BPDC-RB (alone) investigated under similar conditions used for PSE in MeOH/DMF **a**) for 1d-RT, **b**) for 7d-RT, **c**) for 1d-100 °C and **d**) for 7d-100 °C.

Table S1: Fluorescence lifetime decay values obtained for the BPDC-RB alone and BPDC-RB in digested UiO-67 solutions under the same conditions used for PSE.

	BPDC-RB in DMF; τ (ns)		**BPDC-RB in MeOH/DMF; τ (ns)**	
	in absence of UiO-67	in UiO-67*	in absence of UiO-67	in UiO-67*
1d-RT	2.31	2.14	2.19	2.19
7d-RT	2.16	2.18	2.18	2.20
1d-100 °C	2.29	2.11	2.20	2.10
7d-100 °C	2.25	2.12	2.11	2.13
RB alone	2.21		2.17	

*BPDC-RB lifetimes in digested UiO-67 according to the indicated procedure in Fig.S10 b.

4.2. Determination of the BPDC-RB linker exchange ratio.

To determine the amount of incorporated BPDC-RB linker and its exchange ratio after PSE, the fluorescence intensities obtained from the digested UiO-67 crystals were quantified (Fig.S10 c and e). Here, we compared the raw BPDC-RB intensities (measured alone under identical conditions and fit with a linear function, Fig.S13) to the signal obtained from the digested UiO-67 where four different PSE conditions were applied. This comparison of the signals was used to calculate concentrations (based on the linear function

calibration curve) and hence an estimate of the amount of BPDC-RB in the digested UiO-67 was obtained. The PSE efficiency was calculated as the molar ratio between the BPDC-RB and the total linkers (Table S2).

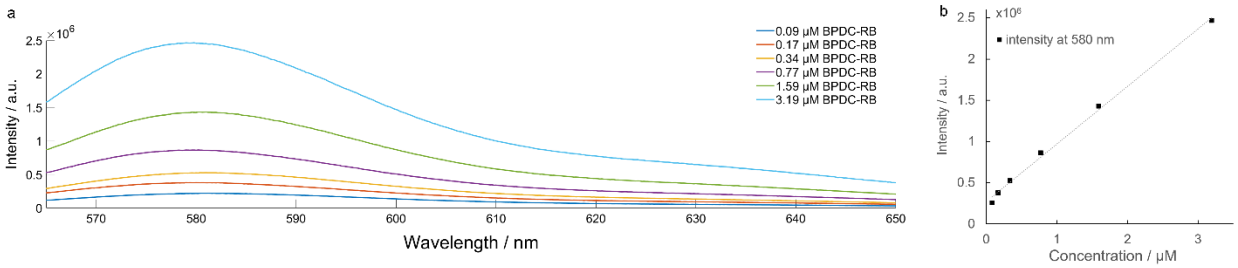

Figure S13: Fluorescence emission of different BPDC-RB concentrations used to estimate the amount of exchanged linker in the digested UiO-67. **a**) Steady state spectra ($\lambda_{excitation}$ = 561 nm) and **b**) fluorescence intensity vs. [BPDC-RB] monitored at 580 nm.

Table S2: Estimated amount of BPDC-RB linker and its exchange ratio in the digested (0.25 mg) UiO-67 crystals studied under four different PSE conditions.

	BPDC-RB in DMF		**BPDC-RB in MeOH/DMF**	
	amount (µg) per 0.25 mg UiO-67	PSE efficiency*	amount (µg) per 0.25 mg UiO-67	PSE efficiency*
1d-RT	0.09	0.09 %	0.76	0.68 %
7d-RT	0.27	0.22 %	2.9	2.6 %
1d-100 °C	0.41	0.35 %	4.9	4.4 %
7d-100 °C	0.65	0.57 %	8.4	7.4 %

* The PSE efficiency was calculated as the molar ratio between the BPDC-RB and the total linkers.

5. Spatial characterization of PSE with 3D fluorescence imaging.

The 3D spatial characterization of PSE was obtained by recording a z-stack of 2D-slices of fluorescence intensity images at height intervals of 500 nm. We analyzed the 3D-fluorescence intensity distribution within the crystal, perpendicular to the surface. This analysis was done in the lateral direction by taking a single z-slice collected at 3 µm above the surface and in the axial direction by taking the same region of interest (ROI) throughout the z-stack (Fig.2). This allowed us to obtain and analyze the 3D penetration depth of the labeled linker. It is worth noting that, for conditions where the label is only bound on or near the surface, the measured spatial distribution will be limited by the diffraction limit of the microscopy (~0.3 µm and ~2 µm for the lateral and axial dimensions, respectively) rather than the actual spatial distribution of the fluorophores (e.g. RB penetration in Fig.S6).

To quantify the PSE, we looked at the fluorescence intensity ratio between a point inside of the crystal (3 µm above the surface) and its surface. We choose 3 µm inside the crystals as the intensity is still high enough to make meaningful comparisons between different conditions. The functionalization of the UiO-67 with BPDC-RB was investigated with different incubation media (DMF and MeOH/DMF solvents) and temperatures (RT and 100 °C). Generally, we observed a very low PSE progression in DMF under all conditions and the only significant amount of linker exchange was observed for 7d-100 °C (Fig.S14). After 7d-100 °C functionalization, a penetration ratio of ~ 7% was observed 3 µm above the surface (Fig.S14 c). In MeOH/DMF, on the other hand, the extent of PSE is significantly higher, especially for longer incubation times at 100 °C, where the penetration ratio 3 µm above surface increased from ~ 14% (after 1d) to ~ 32% (after 7d) (Fig.S14 c).

For incubation in MeOH/DMF, we measured the fluorescence after 1d, 4d, and 7d (Fig. S15). The 1d and 7d images are reproduced from Fig. 3. The additional 4d image and its fluorescence intensity profile show a PSE level between that of 1d and 7d, indicating a gradual progression of PSE on the time frame of 7d.

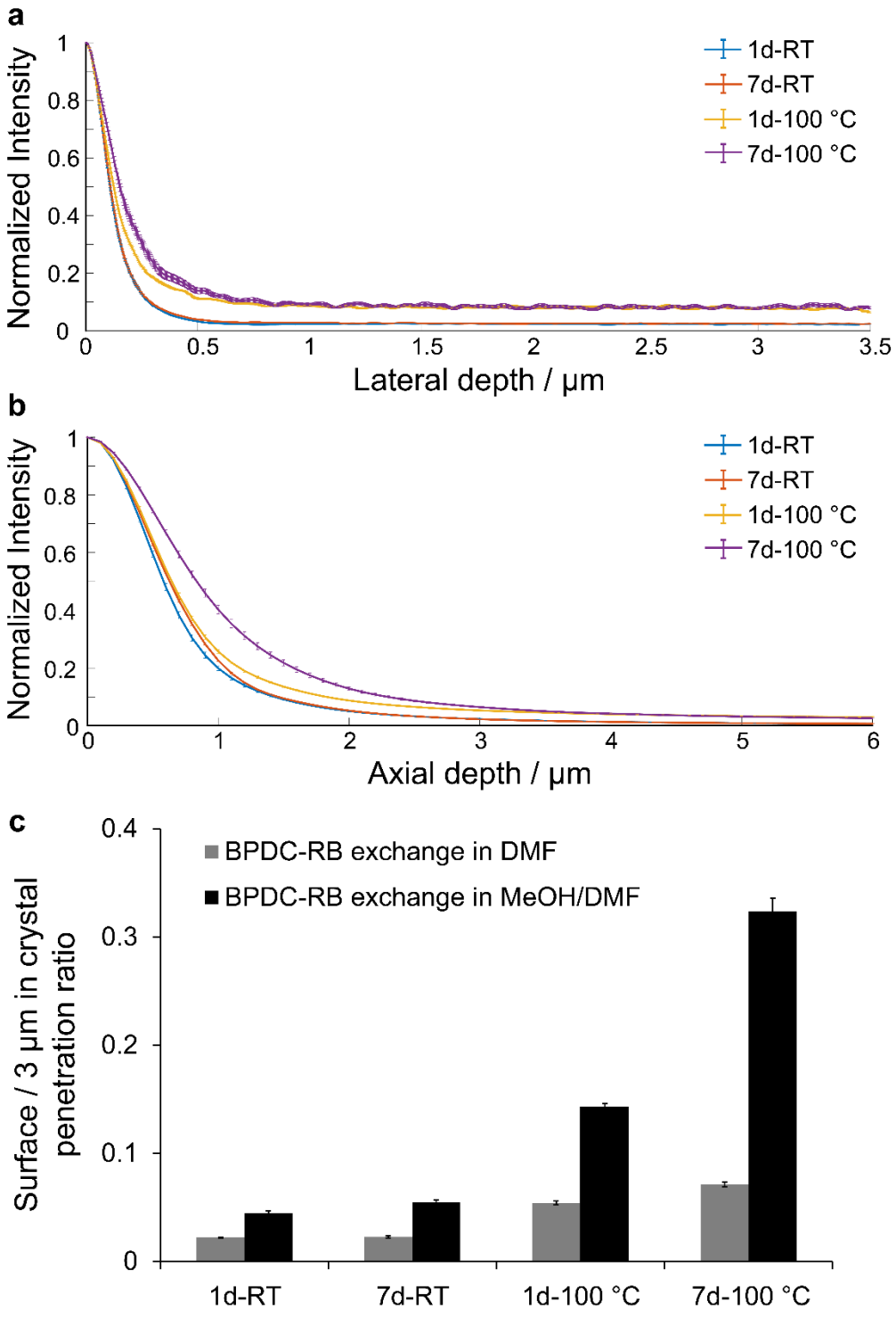

Figure S14: The fluorescence intensity distribution in UiO-67 crystals after PSE in DMF. **a**) Fluorescence intensity profile along lateral direction and (**b**) axial direction (error bars from measurements on 8-10 UiO-67 crystals per condition). **c**) The ratio of fluorescence intensity at 3 µm above surface to the that at the surface (penetration ratio) obtained for UiO-67 crystals after PSE in DMF and MeOH/DMF. The panels of 1d and 7d are reproduced from Fig. 3.

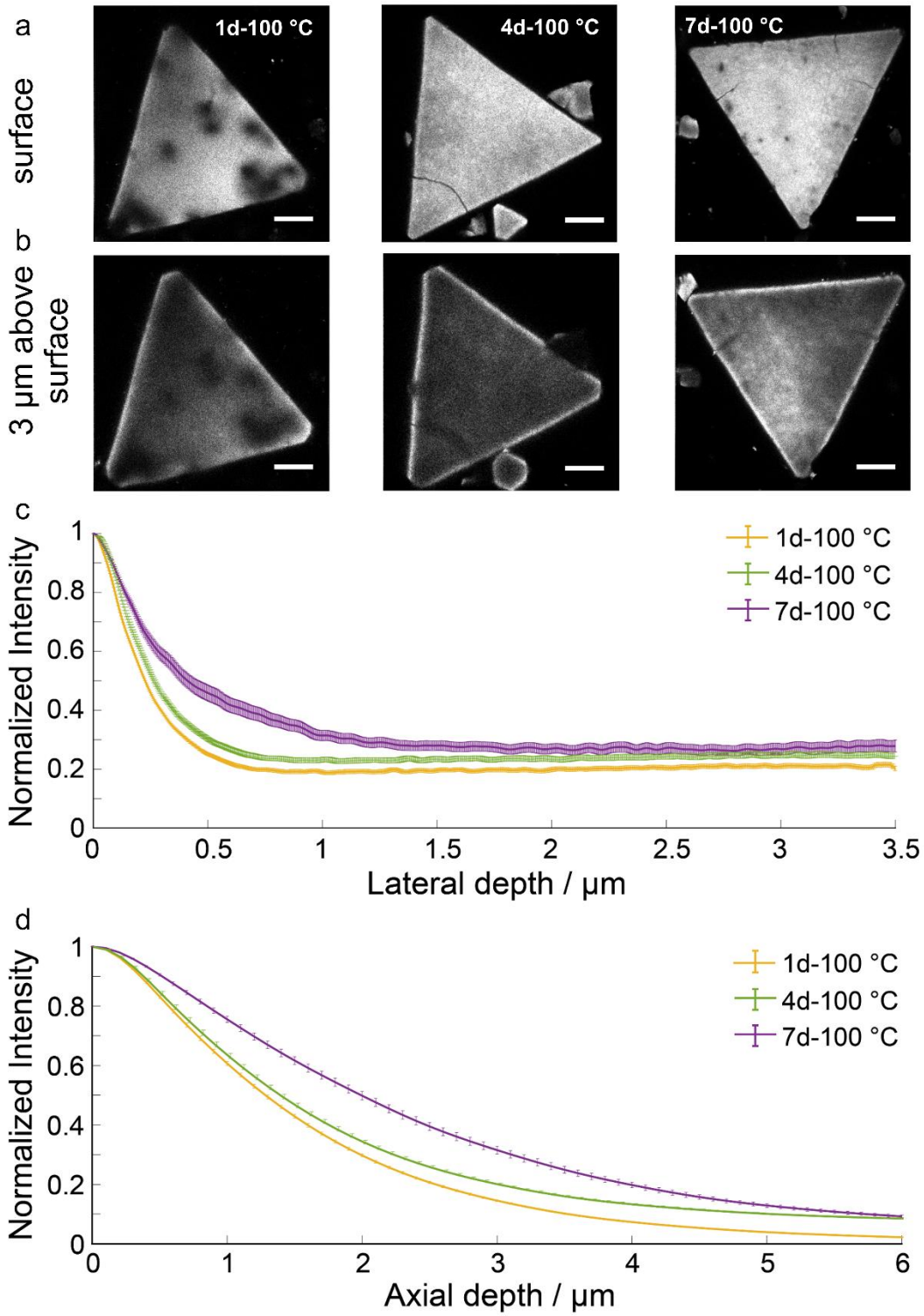

Figure S15: Fluorescence imaging of UiO-67 crystals after PSE in MeOH/DMF for 1d, 4d, and 7d at 100 °C. **a**) Fluorescence images taken at the surface and (**b**) 3 µm above the surface. The scale bar is 15 µm. **c**) Fluorescence intensity profile along lateral and (**d**) axial directions (error bars from measurements on 8-10 UiO-67 crystals per condition).

6. Investigation of defect formation during PSE in MeOH/DMF

To address the PSE induced structural changes, fluorescence lifetime imaging microscopy (FLIM) was performed where the fluorescence lifetime of BPDC-RB was utilized to examine local defect formation after PSE in UiO-67 under different conditions in MeOH/DMF.

UiO-67 after PSE at RT in MeOH/DMF showed significant lifetime differences between 1d and 7d functionalization, where the lifetime decreased from 2.31 ± 0.34 ns after 1d (Fig.S16 c, red) to 1.46 ± 0.45 ns after 7d (Fig.S16 d, yellow-cyan). This would indicate the presence of more detects in the crystal after PSE for 7d. It is worth mentioning that there are minimal differences in the fluorescence lifetime between the crystal surfaces and their interior under RT conditions (Fig.S16-S19), although the low signal in the interior of the crystal makes it more difficult to visualize the lifetime in the image. On the other hand, PSE after 1d-100 °C displayed significant spatial lifetime differences between the crystal surfaces and their interior indicating enhanced defects formation at this elevated temperature (Fig. S16 and S19). Here, a significantly longer lifetime (2.54 ± 0.13 ns, Fig.S16 e, surface, red color) was observed in the crystal interior compared to the lifetime at the surface (1.35 ± 0.20 ns, Fig.S16 e, 4 µm above surface, cyan). This observation correlates well with the fluorescence intensity distribution. This suggests that, as linker exchange advances via the *through-backbone diffusion*, PSE leaves behind a wake of missing linkers. Hence, regions of higher fluorescence intensity where more linker exchange has occurred also have a shorter lifetime due to more defect-induced quenching.

The UiO-67 after PSE for 7d-100 °C resulted in further lifetime quenching compared to the 1d-100 °C functionalization, where a shorter lifetime of 0.89 ± 0.20 ns was measured (Fig.S16 d, blue color). The spatial distribution was much more uniform (Fig.S20). The lack of spatial differentiation, in this case, points towards an equilibrium in defect formation, where defect formation and healing are occurring at similar rates. However, due to the high amount of quenching after 7d, it is very difficult to judge the concentration of defects under such conditions. The high quenching (very short fluorescence lifetimes ~ 1 ns) reduces both the fluorescence lifetime and the photon emission rate. Therefore, a single fluorophore that is - by chance - in a region with low defect concentration, might overwhelm the signal of several dyes that are much closer to a defect and thus quenched even more strongly. Hence, it is possible that we are reaching the limit of sensitivity of our probe.

It is also interesting to note that, for all UiO-67 crystals after PSE for 7d-100 °C, a slight increase in lifetime at the surfaces is observed. This may indicate that defects are being refilled near the surface with the linkers released during linker exchange. The surface would have the highest concentration of released linkers and reannealing of the defects would decrease quenching and result in an increase in lifetime.

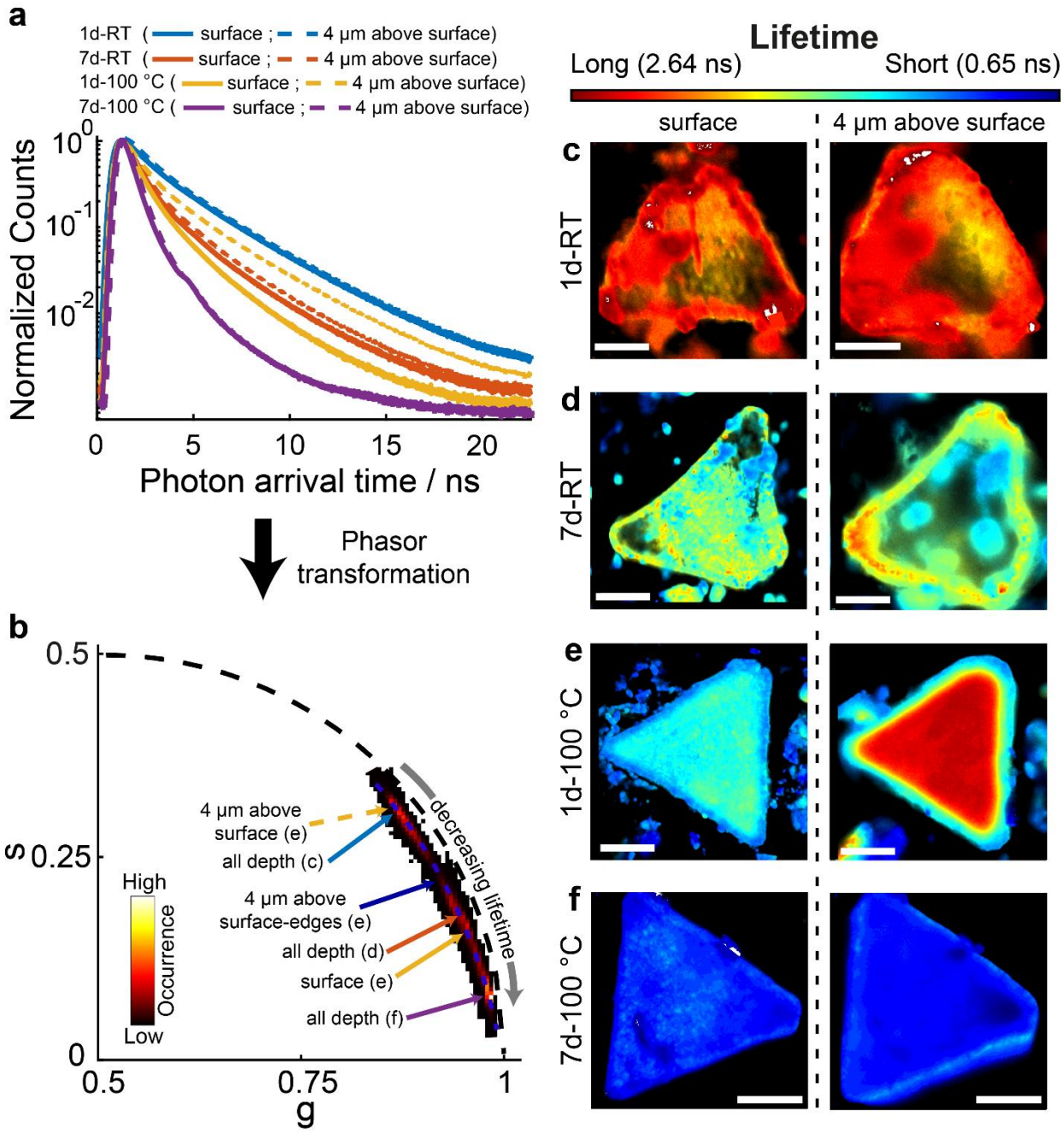

Figure S16: Crystals after PSE under different conditions in MeOH/DMF were characterized using FLIM. **a**) Fluorescence lifetime decays and **b**) the corresponding phasor plot (obtained via the Fourier transformation from the lifetimes in **a**) for the eight FLIM images shown in (**c**-**f**). The color in the phasor plot corresponds to the number of pixels exhibiting the particular phasor value (black indicating the lowest occurrence and yellow indicating the highest occurrence). The dotted-blue line in the phasor plots is used for generating the color table for the fluorescence lifetimes in the FLIM images. **c**-**f**) FLIM images after PSE for 1d-RT (**c**), 7d-RT (**d**), 1d-100 °C (**e**), and 7d-100 °C (**f**). The scale bar is 15 µm.

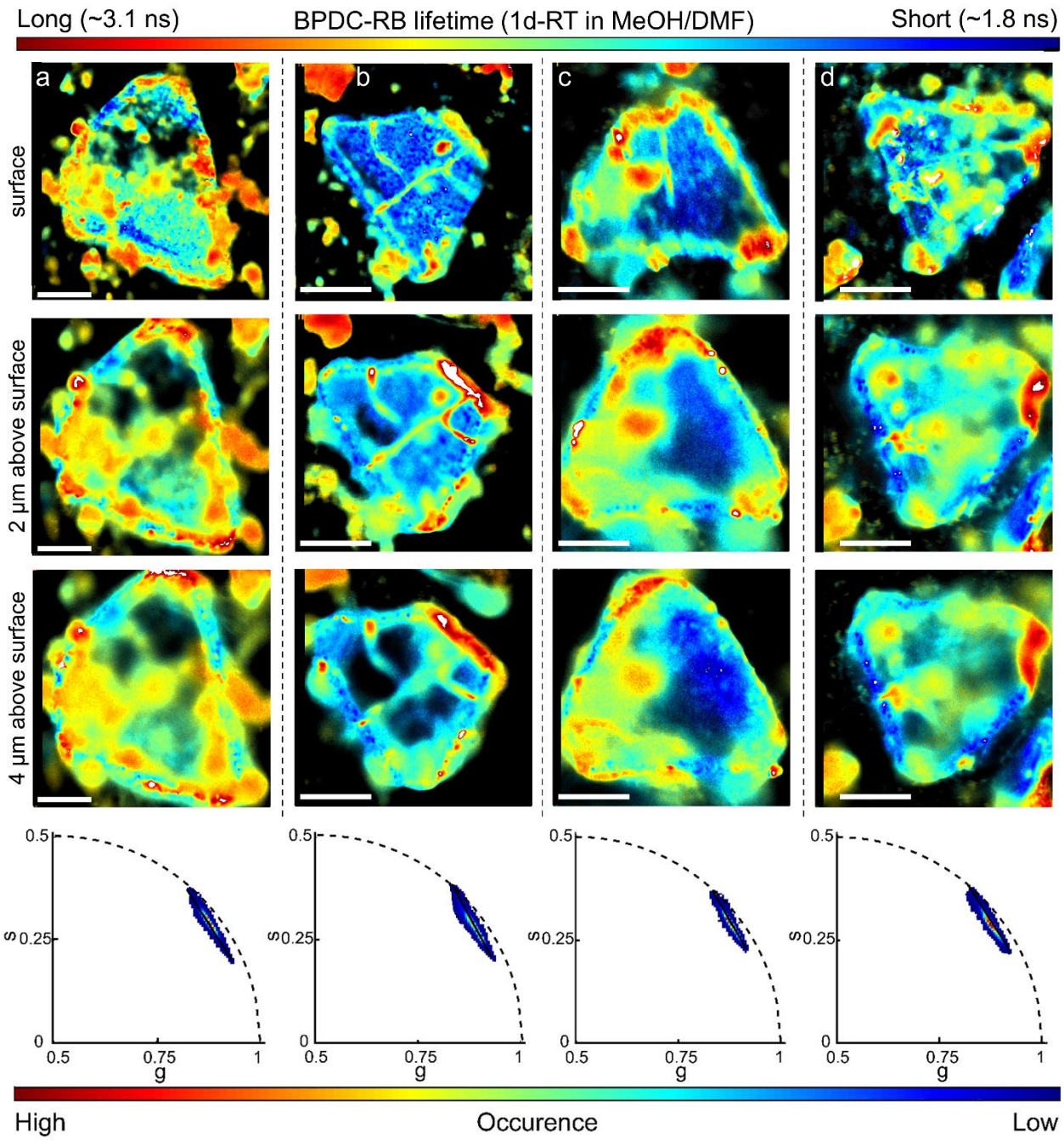

Figure S17: Four crystals after PSE in MeOH/DMF for 1d-RT were characterized using FLIM (panels **a-d**). The scale bar in all images is 15 µm. The last row of each panel shows the corresponding phasor plot of the three FLIM images in panels **a**, **b**, **c** and **d**, respectively. The color in the phasor plots corresponds to the number of pixels exhibiting the particular phasor value (blue indicating the lowest occurrence and red indicating the highest occurrence); see the lower color bar.

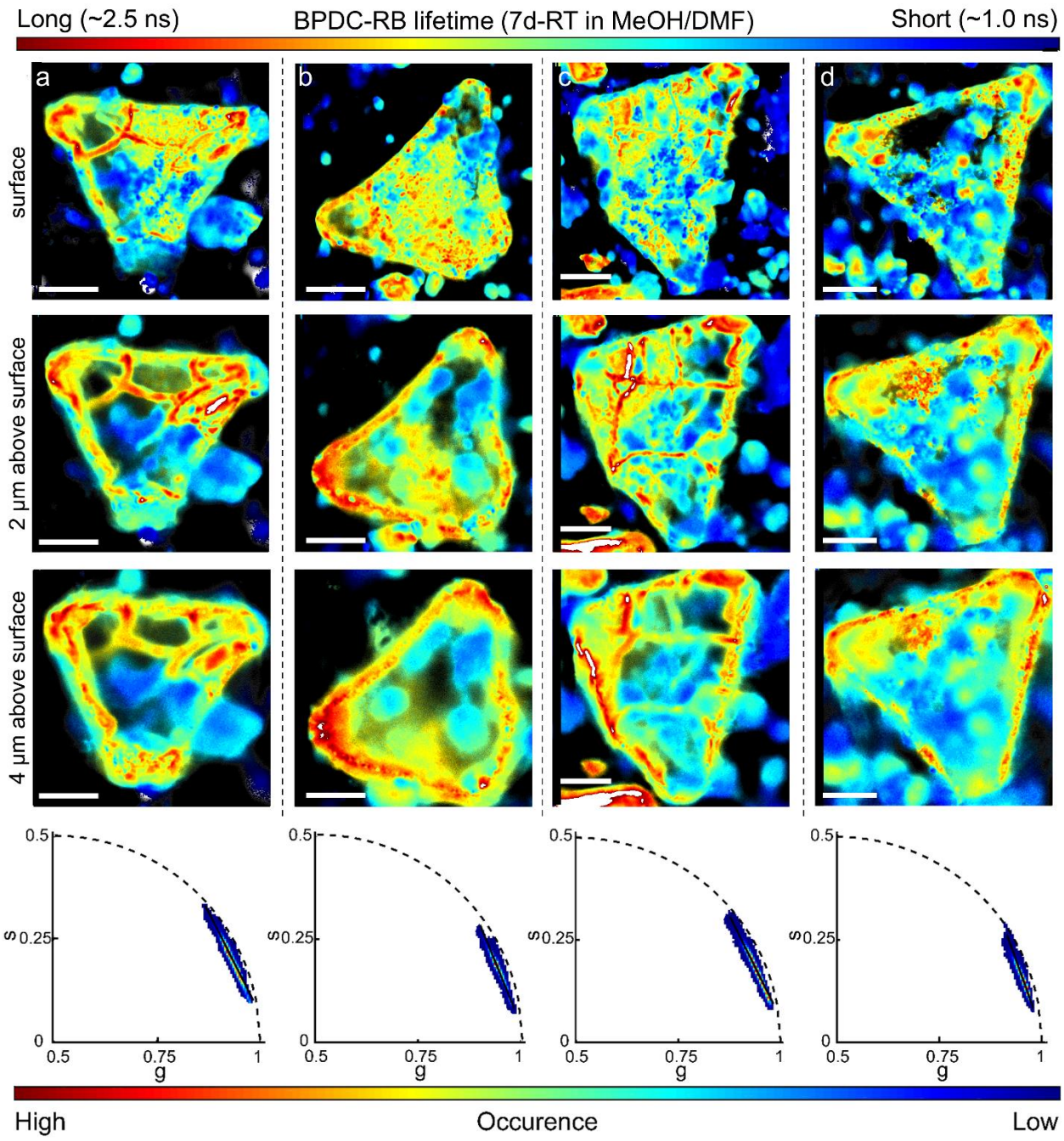

Figure S18: Four crystals after PSE in MeOH/DMF for 7d-RT were characterized using FLIM (panels **a-d**). The scale bar in all images is 15 µm. The last row of each panel shows the corresponding phasor plot of the three FLIM images in panels **a**, **b**, **c** and **d**, respectively. The color in the phasor plots corresponds to the number of pixels exhibiting the particular phasor value (blue indicating the lowest occurrence and red indicating the highest occurrence); see the lower color bar.

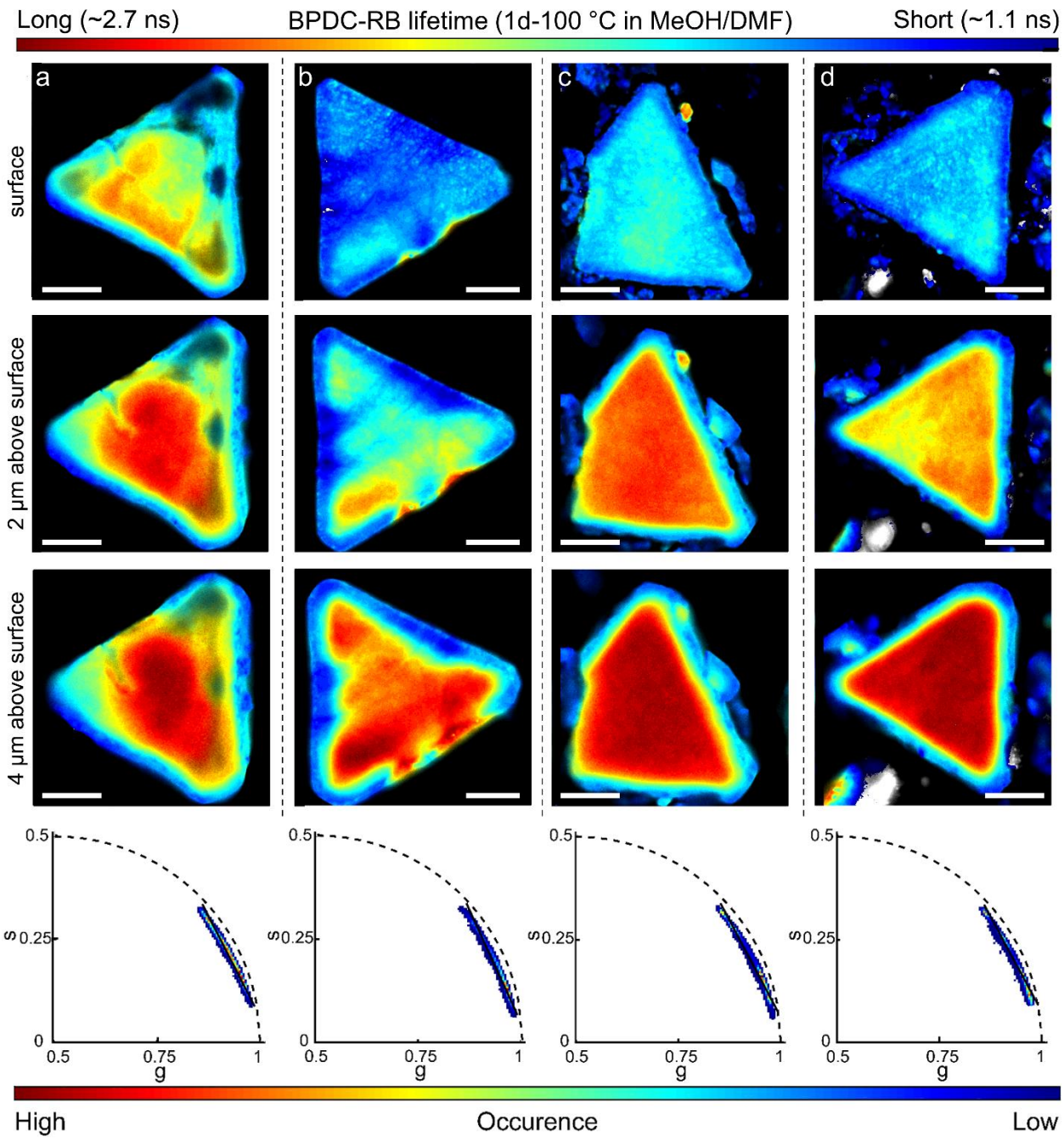

Figure S19: Four crystals after PSE in MeOH/DMF for 1d-100 °C were characterized using FLIM (panels **a-d**). The scale bar in all images is 15 µm. The last row of each panel shows the corresponding phasor plot of the three FLIM images in panels **a**, **b**, **c** and **d**, respectively. The color in the phasor plots corresponds to the number of pixels exhibiting the particular phasor value (blue indicating the lowest occurrence and red indicating the highest occurrence); see the lower color bar.

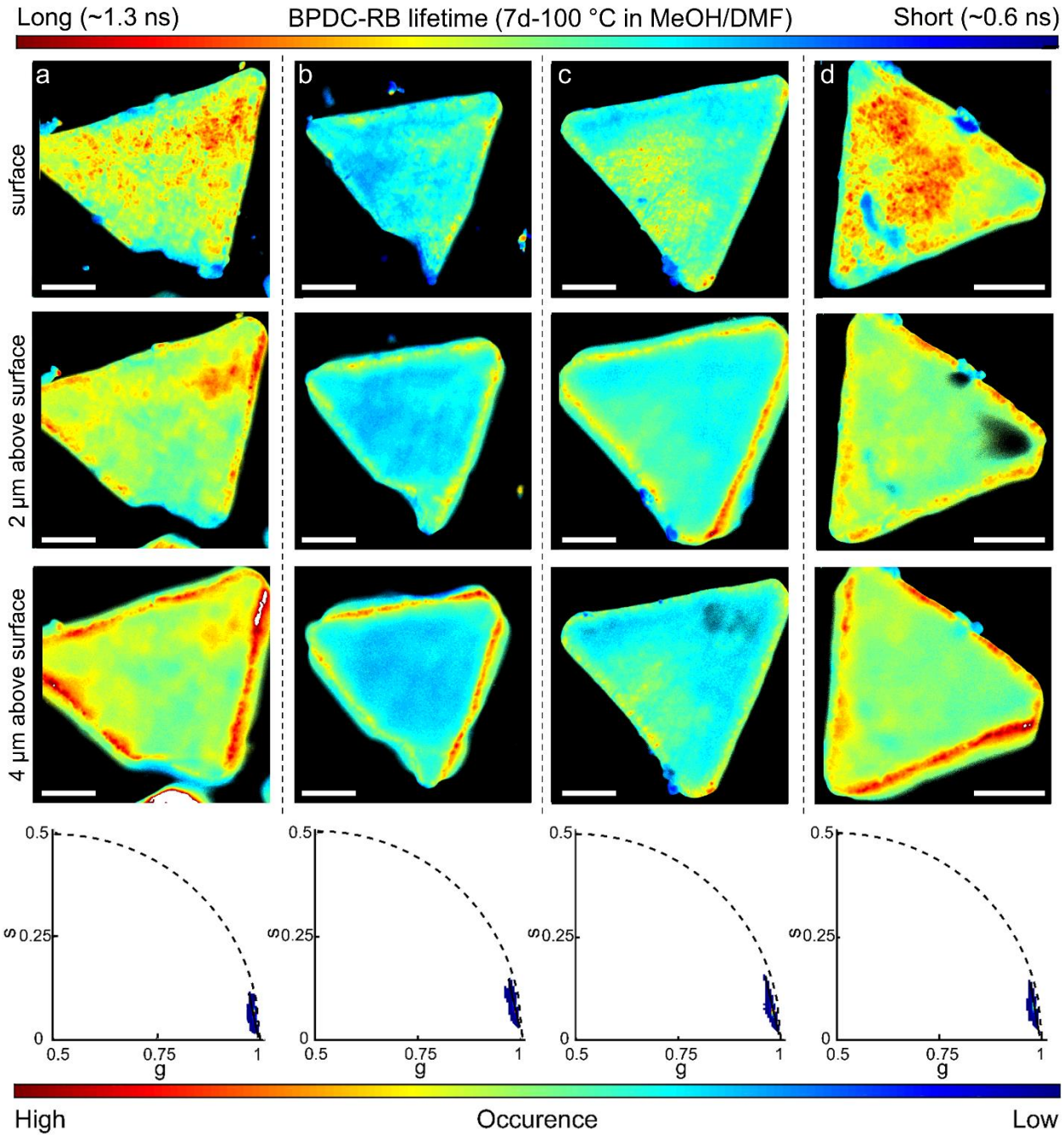

Figure S20: Four crystals after PSE in MeOH/DMF for 7d-100 °C were characterized using FLIM (panels **a-d**). The scale bar in all images is 15 µm. The last row of each panel shows the corresponding phasor plot of the three FLIM images in panels **a**, **b**, **c** and **d**, respectively. The color in the phasor plots corresponds to the number of pixels exhibiting the particular phasor value (blue indicating the lowest occurrence and red indicating the highest occurrence); see the lower color bar.

7. Investigation of defect formation during PSE in DMF

We observed very little differences in lifetime between UiO-67 crystals functionalized with BPDC-RB in DMF for 1d-RT and 7d-RT. A uniform lifetime distribution of 2.91 ± 0.18 ns was observed throughout the whole crystal (Fig.S21 c and d, orange-red). This lifetime is significantly higher than that of BPDC-RB in solvent, indicating that the local environment of the MOF has a stabilizing effect on the fluorophore and thereby reduces the rate of non-radiative transitions, which may also decrease in efficiency when local defects are present. This lifetime is the highest that we have measured, indicating the absence or minimum number of PSE generated defects in these crystals (Fig.S21-S23). Although the autoluminesce of UiO-67 has a longer lifetime of ~ 3.3 ns (as shown in Fig.S8 c and d), its contribution to the measured lifetime is minimal as the fluorescence signal in the crystals is a factor 20-100 higher than the autoluminesce intensity (Fig.S8 a and b). Contrary to the RT experiments, UiO-67 functionalized with BPDC-RB at 100 °C showed interesting spatial lifetime changes. The PSE induced defects in DMF medium at 100 °C displayed an overall shorter lifetime compared to RT. The lifetime value at the surface after 1d-100 °C and 7d-100 °C linker exchange was 2.18 ± 0.23 ns (Fig.S21 e and f, surface, cyan-blue), which suggests that there are more defects generated near the crystal's surface. Interestingly, the PSE induced defects after 1d and 7d (100 °C) are located at the outer surface and differences in lifetime between the surface and the interior were observed (Fig.S21 and S24-S25). A longer lifetime (2.52 ± 0.30 ns, yellowish color) was obtained 4 µm inside the crystal compared to the surface and edges (2.25 ± 0.40 ns, blueish color) (Fig.S21 e and f, 4 µm above surface, yellow-green). The fluorescence intensity distribution observed in DMF after PSE at 100 °C suggests that migration of BPDC-RB from the outside of the crystal to the interior is less efficient than in MeOH/DMF and requires elevated temperatures to initiate. Interestingly, even after PSE in DMF for 7d-100 °C, a spatial distribution in fluorescence lifetime is still present indicating that an equilibration of defects has not yet occurred, in contrast to what was observed for PSE in MeOH/DMF. This is consistent with the even slower linker *through-backbone diffusion* measured in DMF.

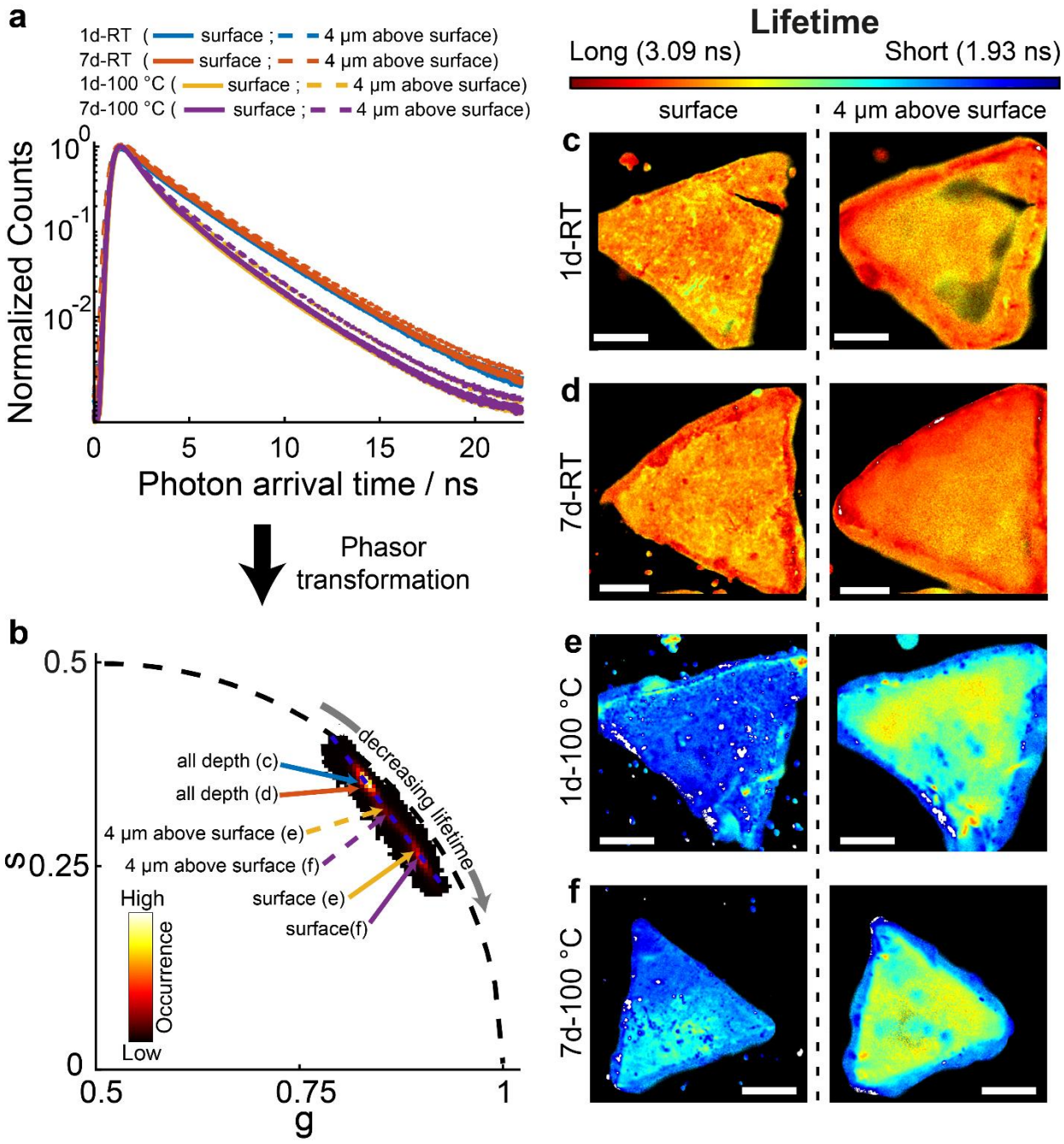

Figure S21: Crystals after PSE under different conditions in DMF were characterized using FLIM. **a**) Fluorescence lifetime decay and **b**) the corresponding phasor plot (obtained via the Fourier transformation from the lifetimes in **a**) for the eight FLIM images shown in (**c**-**f**). The color in the phasor plot corresponds to the number of pixel exhibiting the particular phasor value (black indicating the lowest occurrence and yellow indicating the highest occurrence). The dotted-blue line in the phasor plots is used for generating the color table for the fluorescence lifetimes in the FLIM images. **c**-**f**) FLIM images after PSE for 1d-RT (**c**), 7d-RT (**d**), 1d-100 °C (**e**), and 7d-100 °C (**f**). The scale bar is 15 µm.

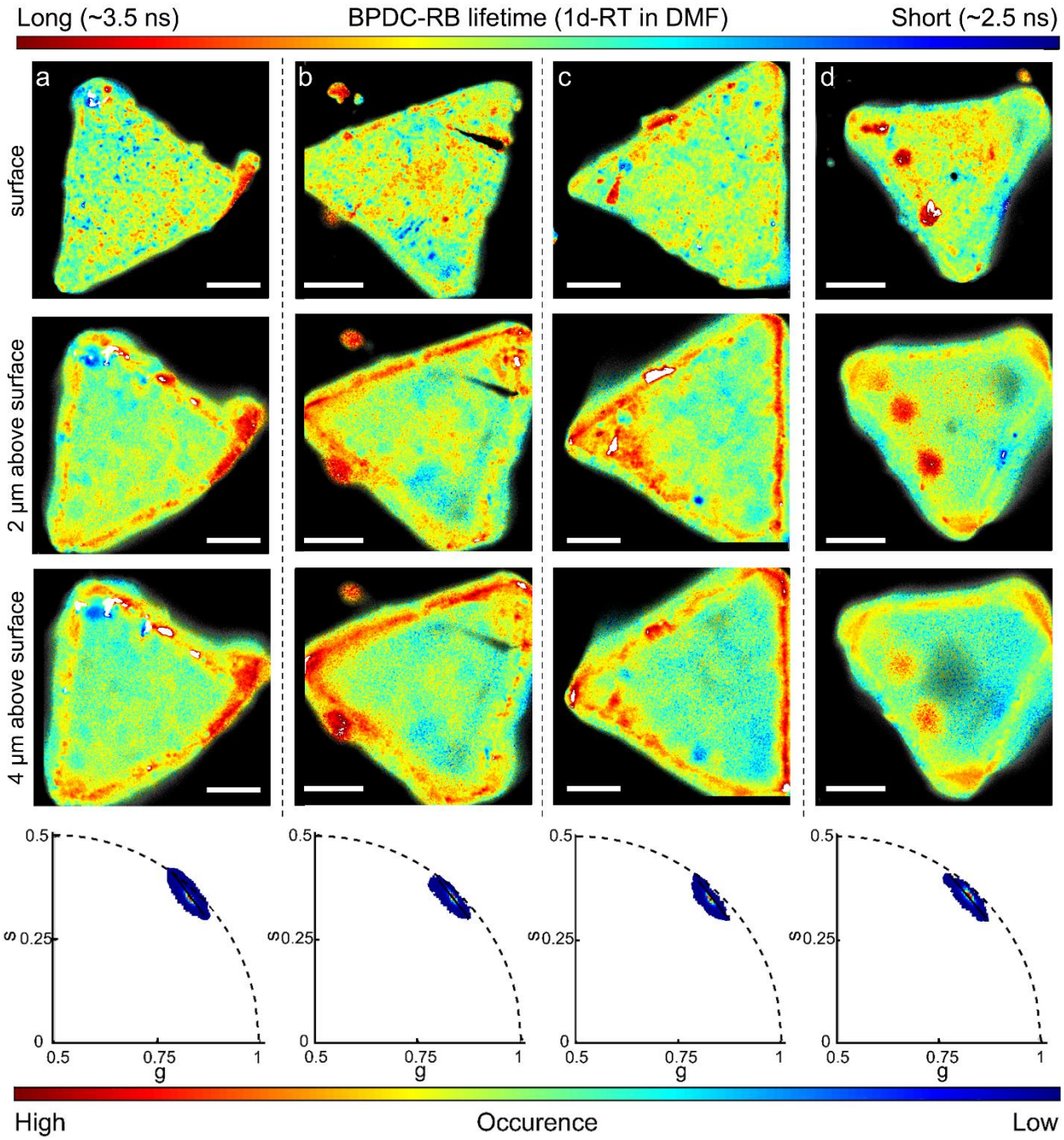

Figure S22: Four crystals after PSE in DMF for 1d-RT were characterized using FLIM (panels **a-d**). The scale bar in all images is 15 µm. The last row of each panel shows the corresponding phasor plot of the three FLIM images in panels **a**, **b**, **c** and **d**, respectively. The color in the phasor plots corresponds to the number of pixels exhibiting the particular phasor value (blue indicating the lowest occurrence and red indicating the highest occurrence); see the lower color bar.

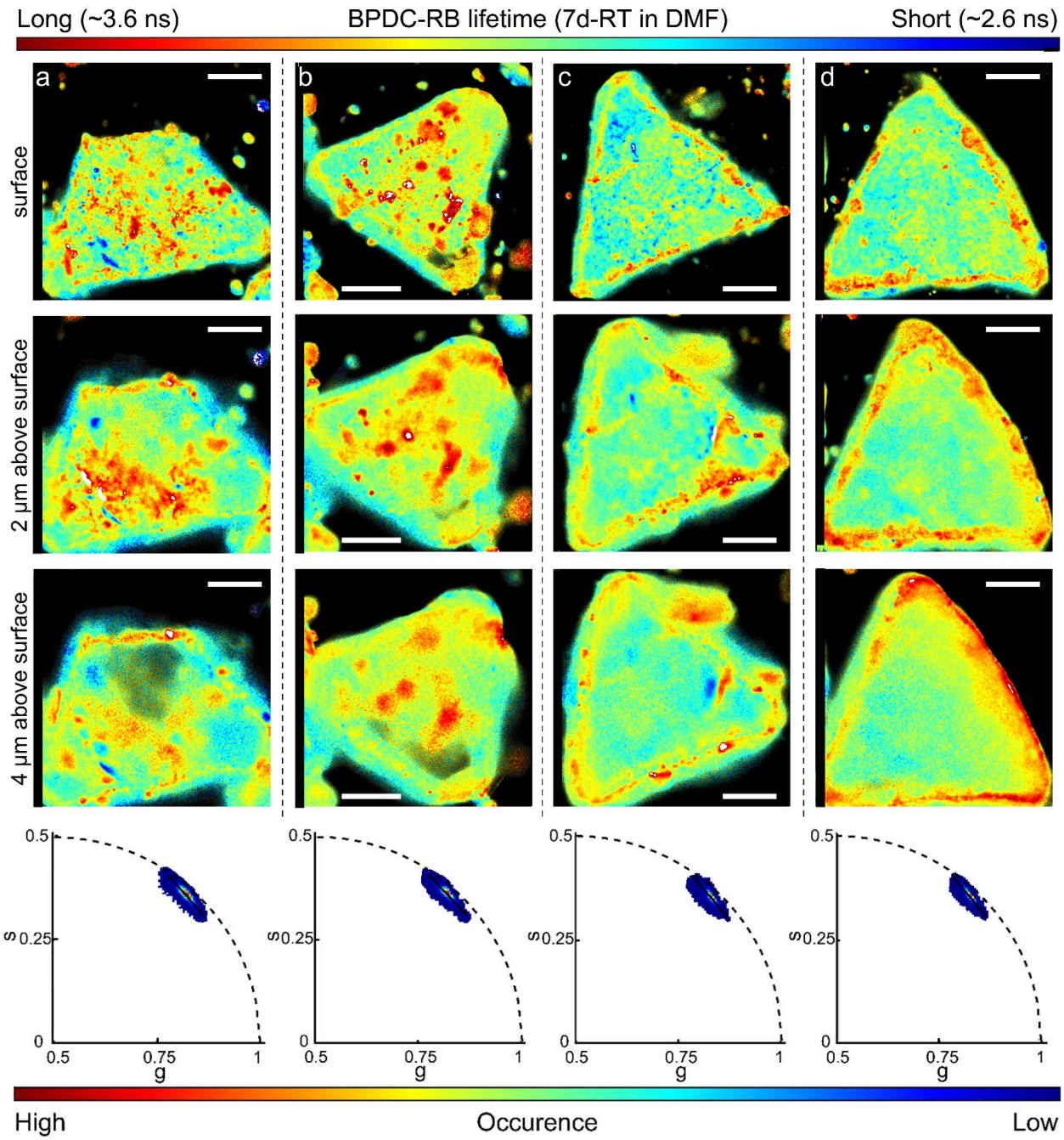

Figure S23: Four crystals after PSE in DMF for 7d-RT were characterized using FLIM (panels **a-d**). The scale bar in all images is 15 µm. The last row of each panel shows the corresponding phasor plot of the three FLIM images in panels **a**, **b**, **c** and **d**, respectively. The color in the phasor plots corresponds to the number of pixels exhibiting the particular phasor value (blue indicating the lowest occurrence and red indicating the highest occurrence); see the lower color bar.

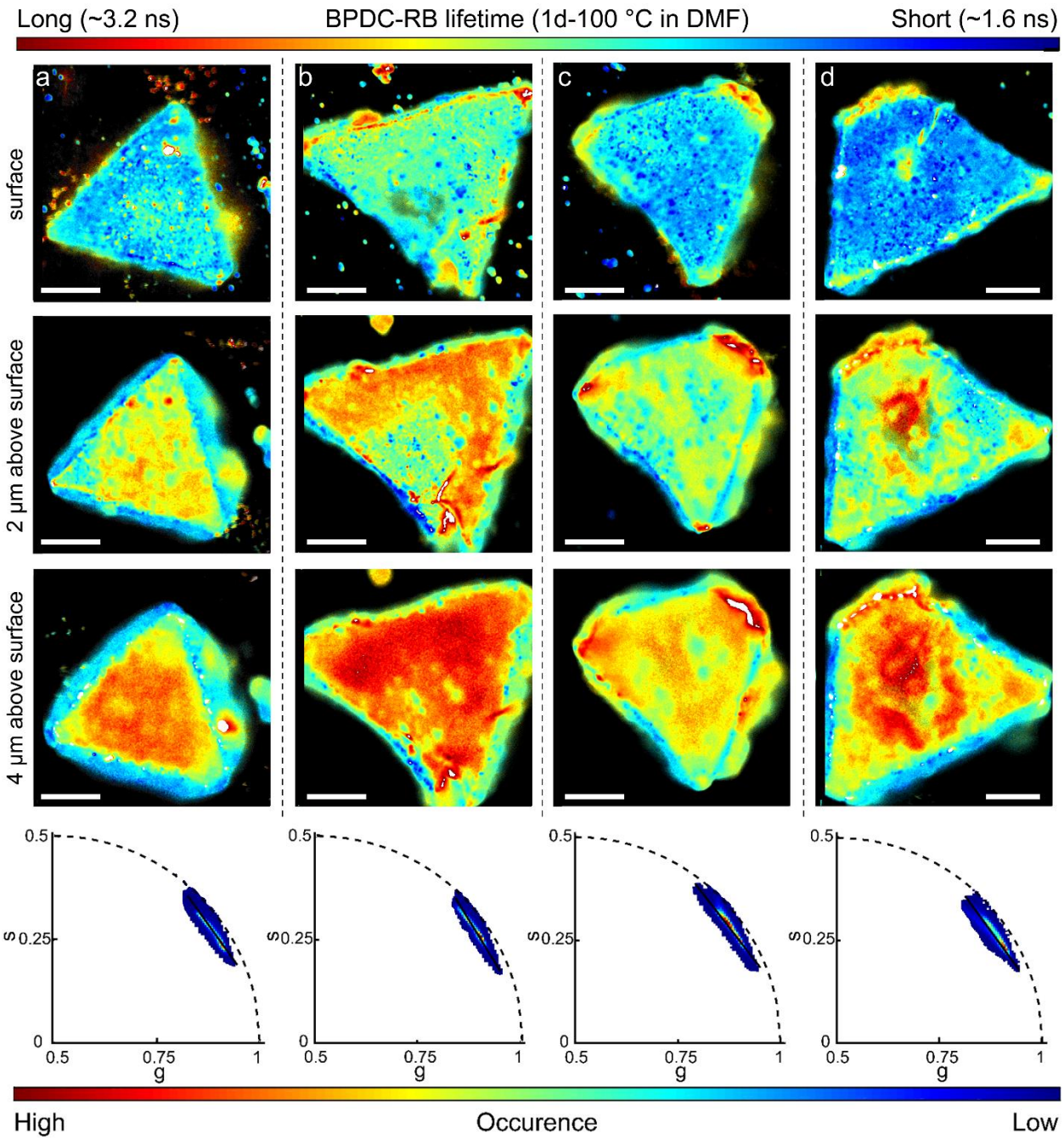

Figure S24: Four crystals after PSE in DMF for 1d-100 °C were characterized using FLIM (panels **a-d**). The scale bar in all images is 15 µm. The last row of each panel shows the corresponding phasor plot of the three FLIM images in panels **a**, **b**, **c** and **d**, respectively. The color in the phasor plots corresponds to the number of pixels exhibiting the particular phasor value (blue indicating the lowest occurrence and red indicating the highest occurrence); see the lower color bar.

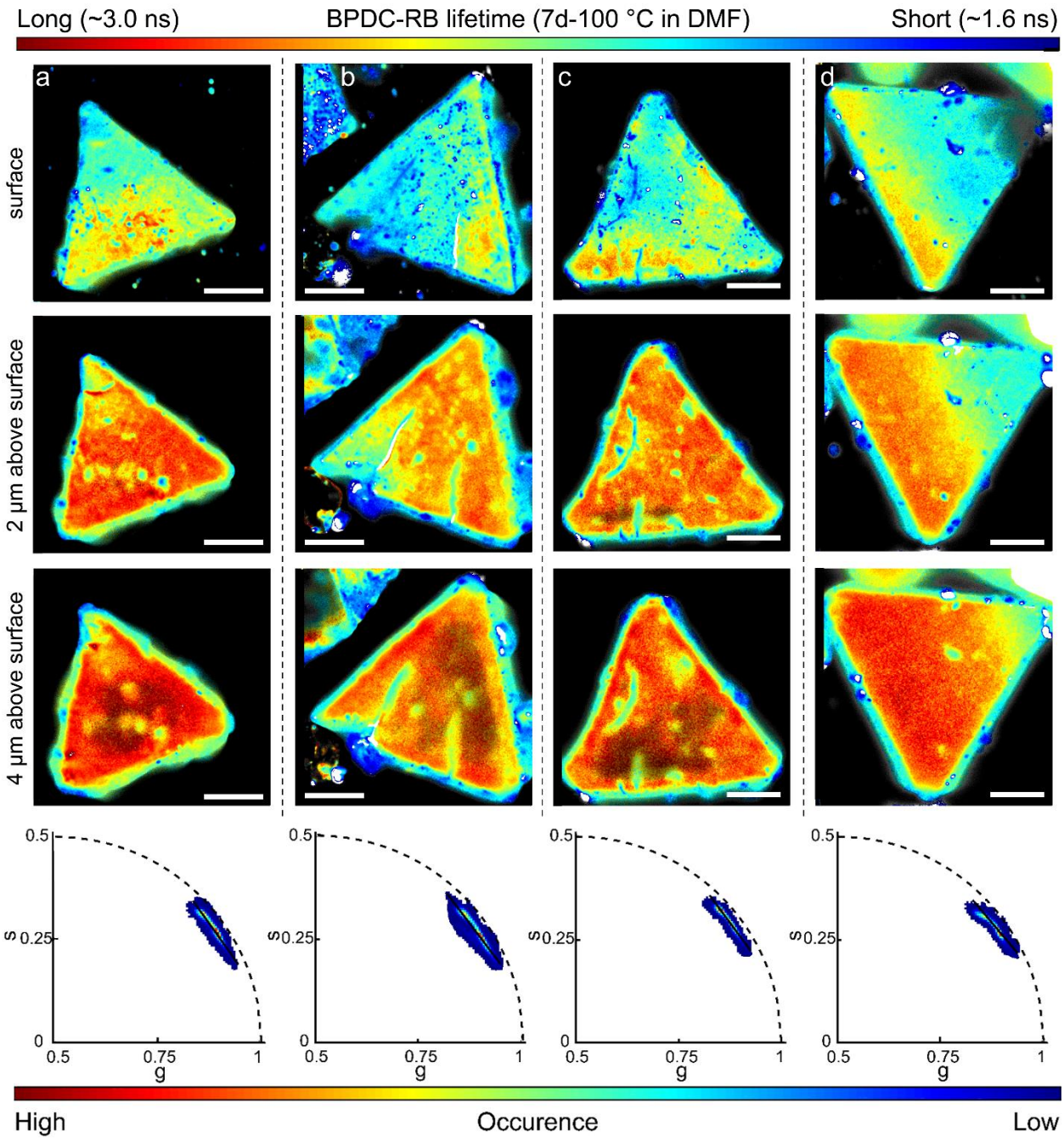

Figure S25: Four crystals after PSE in DMF for 7d-100 °C were characterized using FLIM (panels **a-d**). The scale bar in all images is 15 µm. The last row of each panel shows the corresponding phasor plot of the three FLIM images in panels **a**, **b**, **c** and **d**, respectively. The color in the phasor plots corresponds to the number of pixels exhibiting the particular phasor value (blue indicating the lowest occurrence and red indicating the highest occurrence); see the lower color bar.

References

1. Ko, N.; Hong, J.; Sung, S.; Cordova, K. E.; Park, H. J.; Yang, J. K.; Kim, J., A significant enhancement of water vapour uptake at low pressure by amine-functionalization of UiO-67. *Dalton Trans* **2015,** *44* (5), 2047-51.
2. Schrimpf, W.; Barth, A.; Hendrix, J.; Lamb, D. C., PAM: A Framework for Integrated Analysis of Imaging, Single-Molecule, and Ensemble Fluorescence Data. *Biophys J* **2018,** *114* (7), 1518-1528.
3. Hendrix, J.; Schrimpf, W.; Holler, M.; Lamb, D. C., Pulsed interleaved excitation fluctuation imaging. *Biophys J* **2013,** *105* (4), 848-61.
4. Redford, G. I.; Clegg, R. M., Polar Plot Representation for Frequency-Domain Analysis of Fluorescence Lifetimes. *Journal of Fluorescence* **2005,** *15* (5), 805.
5. Digman, M. A.; Caiolfa, V. R.; Zamai, M.; Gratton, E., The Phasor Approach to Fluorescence Lifetime Imaging Analysis. *Biophysical journal* **2008,** *94* (2), L14-L16.
6. Kaur, G.; Øien-Ødegaard, S.; Lazzarini, A.; Chavan, S. M.; Bordiga, S.; Lillerud, K. P.; Olsbye, U., Controlling the Synthesis of Metal–Organic Framework UiO-67 by Tuning Its Kinetic Driving Force. *Crystal Growth & Design* **2019,** *19* (8), 4246-4251.
7. Cavka, J. H.; Jakobsen, S.; Olsbye, U.; Guillou, N.; Lamberti, C.; Bordiga, S.; Lillerud, K. P., A new zirconium inorganic building brick forming metal organic frameworks with exceptional stability. *J Am Chem Soc* **2008,** *130* (42), 13850-1.